Prepared for submission to JCAP



# Dark matter and halo bispectrum in redshift space: theory and applications

**Héctor Gil-Marín,**[a] **Christian Wagner,**[b] **Jorge Noreña,**[c] **Licia Verde,**[d,e,f] **Will Percival**[a]

[a]Institute of Cosmology & Gravitation, University of Portsmouth, Dennis Sciama Building, Portsmouth PO1 3FX, UK
[b]Max-Planck-Institut für Astrophysik, Karl-Schwarzschild Str. 1, 85741 Garching, Germany
[c]Department of Theoretical Physics and Center for Astroparticle Physics (CAP), 24 quai E. Ansermet, CH-1211 Geneva 4, CH
[d]ICREA Institució Catalana de Recerca i Estudis Avançats. Passeig Lluís Companys 23, E-08010 Barcelona, Spain
[e]Institut de Ciencies del Cosmos, Universitat de Barcelona, IEEC-UB, Marti i Franques 1, 08028, Barcelona, Spain
[f]Institute of Theoretical Astrophysics, University of Oslo, Norway

E-mail: hector.gil@port.ac.uk

**Abstract.** We present a phenomenological modification of the standard perturbation theory prediction for the bispectrum in redshift space that allow us to extend the model to mildly non-linear scales over a wide range of redshifts, $z \leq 1.5$. We test the regime of validity of this new approach with dark matter particles and haloes with two different $\Lambda$CDM cosmologies, both consistent with current data. We find that we can describe the bispectrum of dark matter particles with $\sim 5\%$ accuracy for $k_i \lesssim 0.10\,h/\mathrm{Mpc}$ at $z = 0$, for $k_i \lesssim 0.15\,h/\mathrm{Mpc}$ at $z = 0.5$, for $k_i \lesssim 0.17\,h/\mathrm{Mpc}$ at $z = 1.0$ and for $k_i \lesssim 0.20\,h/\mathrm{Mpc}$ at $z = 1.5$. We apply this new formula to recover the bias parameters, logarithmic growth rate $f$ and $\sigma_8$, by combining the redshift space power spectrum monopole and quadrupole with the bispectrum monopole for both dark matter particles and haloes. We find that the combination of these three statistics can break the degeneracy between $b_1$, $f$ and $\sigma_8$. For dark matter particles the new model can be used to recover $f$ and $\sigma_8$ with $\sim 1\%$ systematic accuracy. For dark matter haloes we find that $f$ and $\sigma_8$ present larger systematic shifts, $\sim 10\%$. The systematic offsets arise because of limitations in the modelling of the interplay between bias and redshift space distortions, and represent a limitation as the statistical errors of forthcoming surveys reach this level. Conveniently, we find that these residual systematics are mitigated for combinations of parameters. In particular, the quantity $f\sigma_8$ is still recovered with $\sim 1\%$ accuracy. The improvement on the modeling of the bispectrum presented in this paper will be useful for extracting information from current and future galaxy surveys.

## Contents



## 1 Introduction

Over the last decade advances in astronomical spectroscopy and photometry of large samples of galaxies have allowed the galaxy distribution to be measured to unprecedented accuracy. The analysis of the resulting maps has yielded constraints on the growth rate of structures, the Universe expansion history as well as on cosmological parameters.

The successful measurement of cosmological parameters relies on both the accuracy of the theoretical models as well as the precision of the statistics used. In the past, the precision of the measurements was poor and a $\sim 10\%$ statistical error on the measurement of the power spectrum and even higher on the bispectrum was the limiting factor for discriminating among models and theories. However, current and forthcoming surveys (BOSS [2][1], WiggleZ [3][2], DES [4][3], EUCLID [5][4]) are rapidly approaching to the 1% statistical precision for two-point statistics, and are constraining higher-order statistics with similar jump in precision. This level of precision is comparable to the accuracy of the theoretical models that have been developed. Consequently, a large effort has been put into improving the theory, proceeding in different directions. The first step is to upgrade the modeling of the statistics of dark matter in real space [6–10]. The second is to improve the bias model in order to describe accurately how the galaxies trace dark matter, including non-linear, non-local and non-Gaussian terms [11–13]. The third is to accurately model the mapping from real to redshift space statistics [14–17]. Combining these improvements leads to a model to describe the 2-point statistics with accuracy close to 1%. Although some progress have been made [18–27], we have not seen a similar improvement for higher-order statistics.

Redshift space distortions (RSD), mean that the galaxy distribution observed in spectroscopic surveys is distorted along the line of sight. These distortions depend on the growth rate of structures,

[1]Baryon Oscillator Spectroscopic Survey: http://www.sdss3.org/surveys/boss.php
[2]WiggleZ Dark Energy Survey : http://wigglez.swin.edu.au/
[3]Dark Energy Survey: http://www.darkenergysurvey.org/
[4]EUCLID: http://www.euclid-ec.org/

and therefore offer a complementary technique (to those based on the cosmic expansion history) to measure the matter content and to test gravity [28–30]. However, the accuracy of these tests relies on the ability of the theoretical models to describe correctly the power spectrum and bispectrum in redshift space. In a previous paper [1] we presented an improved phenomenological formula that was able to predict the dark matter bispectrum in real space with a 5% precision up to scales of $k \leq 0.4\,h/\mathrm{Mpc}$ at $z \leq 1.5$. As a natural continuation, we now extend that formula to redshift space, making the model closer to observational data and thus useful to test gravity as well as cosmology.

We use a suite of N-body simulations that consists of 60 independent realisations with a total effective volume of $\sim 829\,[\mathrm{Gpc}/h]^3$ to constrain the free parameters of the new formula using the measurements of the dark matter redshift space bispectrum monopole. With such a large volume, we ensure that the statistical errors are much smaller than those of current or forthcoming surveys. Thus, we can safely quantify the systematic shifts that the fitting formula may introduce. We also use the obtained formulae to model the bispectrum of dark matter haloes in redshift space, and to recover parameters of cosmological interest such as the logarithmic growth rate of structure, $f$ and the amplitude of the (linear) power spectrum $\sigma_8$. Comparing the recovered values to the input ones, we can quantify any possible systematics.

This paper is organized as follows. In § 2 we present the state-of-the art theoretical formulae for the 2- and 3-point statistics in Fourier space. In § 3 we detail the simulations we use to test these formulae and we also introduce the estimator we use for extracting information from power spectrum and bispectrum measurements. In § 4 we present the power spectrum multipole measurements from simulations. In § 5 we present the improved fitting formula for the dark matter bispectrum and we compare it to standard perturbation theory predictions. In § 6 we compare how the new formula is able to describe the halo bispectrum. In § 7 we show the ability of the formula for recover the biases and growth factor for both dark matter particles and haloes. Finally in § 8 we discuss the conclusions of this paper.

## 2 Theory

The matter density power spectrum, $P_{\delta\delta}$, and bispectrum, $B_\delta$, are the two- and three-point correlation functions in Fourier space,

$$\langle \delta(\mathbf{k})\delta(\mathbf{k}')\rangle \equiv (2\pi)^3\delta^D(\mathbf{k}+\mathbf{k}')P_{\delta\delta}(\mathbf{k}), \tag{2.1}$$

$$\langle \delta(\mathbf{k}_1)\delta(\mathbf{k}_2)\delta(\mathbf{k}_3)\rangle \equiv (2\pi)^3\delta^D(\mathbf{k}_1+\mathbf{k}_2+\mathbf{k}_3)B_\delta(\mathbf{k}_1,\mathbf{k}_2), \tag{2.2}$$

where $\delta(\mathbf{k}) \equiv \int d^3\mathbf{x}\,\delta(\mathbf{x})\exp(-i\mathbf{k}\cdot\mathbf{x})$ is the Fourier transform of the dark matter overdensity field, $\delta(\mathbf{x}) \equiv \rho(\mathbf{x})/\bar{\rho}-1$, $\rho$ is the dark matter density and $\bar{\rho}$ its mean value; $\delta^D$ is the Dirac delta distribution and $\langle\ldots\rangle$ the ensemble average (or average over different realisations). Note that the bispectrum function is only defined when the 3 $\mathbf{k}$-vectors form a closed triangle. Also, we identify the bispectrum with the real part of the left hand side of equation 2.2. When the distribution of matter is isotropic, the bispectrum is independent of the particular orientation of the triangles. In this case, we can write $B(\mathbf{k}_1,\mathbf{k}_2) \equiv B(k_1,k_2,k_3)$, where $\mathbf{k}_3 \equiv -\mathbf{k}_1-\mathbf{k}_2$.

In order to link the $n$-point statistics for haloes (the same applies to any dark matter tracer) to that of the mass, we need to introduce a bias model. In this paper, we opt for the halo bias model proposed by [12], which is able to account for both non-linearities and non-localities. Recently, it has been shown that gravitational evolution can induce non-local terms in the halo distribution. These non-local terms appear as a second-order correction for the halo power spectrum. However, for the bispectrum non-localities contribute to leading order. Thus, it is essential to have a bias model that is able to account for these corrections to the halo bispectrum, even at large scales. According to this model, the halo density field is,

$$\delta_\mathrm{h}(\mathbf{x}) = b_1\delta(\mathbf{x}) + \frac{1}{2}b_2[\delta(\mathbf{x})^2-\sigma_2] + \frac{1}{2}b_{s^2}[s(\mathbf{x})^2-\langle s^2\rangle] + \text{higher order terms} \tag{2.3}$$

where $\sigma_2$ and $\langle s^2 \rangle$ ensure the condition $\langle \delta_h \rangle = 0$. Non-linearities are included in $\delta(\mathbf{x})^2$, whereas the non-localities are described by the tidal tensor term $s(\mathbf{x})$,

$$s(\mathbf{x}) \equiv s_{ij}(\mathbf{x}) s_{ij}(\mathbf{x}), \tag{2.4}$$

$$s_{ij}(\mathbf{x}) = \partial_i \partial_j \Phi(\mathbf{x}) - \delta^{\rm Kr}_{ij} \delta(\mathbf{x}), \tag{2.5}$$

where $\Phi(\mathbf{x})$ is the gravitational potential, $\nabla^2 \Phi(\mathbf{x}) = \delta(\mathbf{x})$, and $\delta^{\rm Kr}_{ij}$ is the Kronecker delta. The relation between dark matter and halo over-densities is parametrised through the bias parameters: the linear bias term $b_1$, the non-linear bias term $b_2$ , and the non-local bias term $b_{s^2}$. Most higher-order terms only contribute at small scales and we do not consider them here. However, there are some that can be renormalised as large-scale contributions and therefore must be considered for consistency. We will come back to this point in § 2.1. For $b_1 = 1$, $b_2 = 0$, $b_{s^2} = 0$ and null third order biases, we recover a local and linear bias of unity (i.e., no bias) which applies to the dark matter.

In order to have an expression for the halo bias model in $k$-space we Fourier transform Eq. 2.3,

$$\begin{aligned} \delta_{\rm h}(\mathbf{k}) = & \, b_1 \delta(\mathbf{k}) + \frac{1}{2} b_2 \int \frac{d\mathbf{q}}{(2\pi)^3} \delta(\mathbf{q}) \delta(\mathbf{k}-\mathbf{q}) + \\ & + \frac{1}{2} b_{s^2} \int \frac{d\mathbf{q}}{(2\pi)^3} \delta(\mathbf{q}) \delta(\mathbf{k}-\mathbf{q}) S_2(\mathbf{q}, \mathbf{k}-\mathbf{q}) + \text{higher order terms} \end{aligned} \tag{2.6}$$

where

$$S_2(\mathbf{q}_1, \mathbf{q}_2) \equiv \frac{(\mathbf{q}_1 \cdot \mathbf{q}_2)^2}{(q_1 q_2)^2} - \frac{1}{3} \tag{2.7}$$

is defined from the Fourier transform of the tidal tensor,

$$s^2(\mathbf{k}) \equiv \int d^3\mathbf{x} \, s^2(x) \exp(-i\mathbf{k}\cdot\mathbf{x}) = \int \frac{d\mathbf{k}'}{(2\pi)^3} S_2(\mathbf{k}', \mathbf{k}-\mathbf{k}') \delta(\mathbf{k}') \delta(\mathbf{k}-\mathbf{k}'). \tag{2.8}$$

From the bias relation of Eq. 2.6, we now derive the expressions for the halo power spectrum and bispectrum.

### 2.1 Halo power spectrum

The halo power spectrum, $P_{{\rm h},\delta\delta}(k)$, can be written as a function of the statistical moments of dark matter [12, 31],

$$\begin{aligned} P_{{\rm h},\delta\delta}(k) = & \, b_1^2 P_{\delta\delta}(k) + 2 b_2 b_1 P_{b2,\delta}(k) + 2 b_{s^2} b_1 P_{bs2,\delta}(k) + b_2^2 P_{b22}(k) + \\ & + 2 b_2 b_{s^2} P_{b2s2}(k) + b_{s^2}^2 P_{bs22}(k) + 2 b_1 b_{3{\rm nl}} \sigma_3^2(k) P^{\rm lin}(k), \end{aligned} \tag{2.9}$$

where $P^{\rm lin}$ is the linear power spectrum. The definitions of the power spectra quantities, $P_{b2,\delta}$, $P_{bs2,\delta}$, $P_{b22}$, $P_{b2s2}$, $P_{bs22}$ and $\sigma_3^2$ can be found e.g., in [31]. Note that the contribution regulated by $b_{3{\rm nl}}$, does not appear explicitly in Eq. 2.6. This contribution arises from higher-order terms, but can be renormalized to be proportional to the linear power spectrum, which makes its contribution relevant at large scales [12].

In this paper we assume that the non-local bias terms are given by their first-order predictions in perturbation theory: $b_{s^2} = -4/7(b_1 - 1)$[32, 33] and $b_{3{\rm nl}} = 32/315(b_1 - 1)$ [13, 31], which have been demonstrated to be a good approximation to N-body simulations results. Although $b_1$ and $b_2$ could also be estimated using the peak background split formalism for a particular halo population, in this paper we treat them as free parameters.

In order to describe the halo power spectrum and bispectrum in redshift space, we need to incorporate the information of the velocity components into the formalism. $\theta(\mathbf{k})$ is the usual variable that accounts for the peculiar velocities of dark matter particles, $\theta(\mathbf{k}) \equiv [-i\mathbf{k}\cdot\mathbf{v}_k]/[af(a)H(a)]$, where $a$ is the scale factor, $H$ the Hubble parameter, $f$ the logarithmic growth factor $d\ln\delta/d\ln a$, and $\mathbf{v}_k$

the $k$-space components of the velocity. Two power spectra can be defined using the dark matter velocity field $\theta$,

$$\langle \delta(\mathbf{k})\theta(\mathbf{k}')\rangle \equiv (2\pi)^3\delta^D(\mathbf{k}+\mathbf{k}')P_{\delta\theta}(\mathbf{k}), \tag{2.10}$$

$$\langle \theta(\mathbf{k})\theta(\mathbf{k}')\rangle \equiv (2\pi)^3\delta^D(\mathbf{k}+\mathbf{k}')P_{\theta\theta}(\mathbf{k}), \tag{2.11}$$

where $P_{\delta\theta}$ and $P_{\theta\theta}$ are the density-velocity and the velocity-velocity power spectra, respectively, for dark matter. In this paper we assume that the velocity fields are the same for dark matter and haloes (i.e., no velocity bias). Thus, the cross $\delta\theta$ power spectrum for haloes can be written as,

$$P_{h,\delta\theta}(k) = b_1 P_{\delta\theta}(k) + b_2 P_{b2,\theta}(k) + b_{s^2} P_{bs2,\theta}(k) + b_{3\mathrm{nl}}\sigma_3^2(k)P^{\mathrm{lin}}(k). \tag{2.12}$$

As for Eq. 2.9, the power spectra terms can be found in [31].

According to [11, 16] (TNS model hereafter), the density halo power spectrum in redshift space can be expressed as a function of density and velocity galaxy statistics in real space,

$$\begin{aligned} P_h^{(s)}(k,\mu) \;=\; & D^P_{\mathrm{fog}}(k,\mu;\sigma^P_{\mathrm{fog}})\left[P_{g,\delta\delta}(k) + 2f\mu^2 P_{g,\delta\theta}(k) + f^2\mu^4 P_{\theta\theta}(k) + \right. \\ & \left. +\; b_1^3 A(k,\mu,f/b_1) + b_1^4 B(k,\mu,f/b_1)\right]. \end{aligned} \tag{2.13}$$

The definitions of the $A$ and $B$ terms can be found in [16] and only incorporate first-order corrections, and consequently only depend on $b_1$. Higher-order corrections would include $b_2$, but in this paper we ignore their contribution, which is assumed to be subdominant in the studied regime. The factor $D^P_{\mathrm{fog}}(k,\mu,\sigma^P_{\mathrm{fog}})$ was originally introduced to account for the fully non-linear damping caused by the velocity dispersion of sub-haloes, commonly known as the Fingers of God (FoG) effect. For a haloes-without-structure scenario, no internal velocity dispersion is expected and this term should be set to unity. Previous studies of this model [11] have shown that this term is actually needed to describe accurately the halo power spectrum which does not have FoG. The requirement of a FoG term for describing haloes is therefore physically paradoxical. However, we should think of the damping term in the model of Eq. 2.13 as a general damping required to correct the model for non-linear effects. As a practical solution, we therefore allow a $\sigma^P_{\mathrm{fog}}$-term for describing the halo power spectrum. The physical meaning of this term *is not* a internal velocity dispersion, but an effective parameter that improves the description of the model. We parametrize the damping term through a one-free-parameter formula of Lorentzian type [34, 35],

$$D^P_{\mathrm{fog}}(k,\mu,\sigma^P_{\mathrm{fog}}[z]) \;=\; \left(1 + k^2\mu^2\sigma^P_{\mathrm{fog}}[z]^2/2\right)^{-2} \tag{2.14}$$

with $\sigma^P_{\mathrm{fog}}(z) \equiv \sigma^P_0(z)f(z)D(z)$.

In this work, the dark-matter real-space statistics of Eqs. 2.1, 2.10, 2.11, are given by the 2-loop resummed perturbation theory model described in [36] (2LRPT model hereafter). This model has been shown in [36] to describe $P_{\delta\delta}$ within 2% accuracy up to $k = 0.11\,h/\mathrm{Mpc}$ for $z = 0$; $k = 0.15\,h/\mathrm{Mpc}$ for $z = 0.5$; $k = 0.22\,h/\mathrm{Mpc}$ for $z = 1$; $k > 0.25\,h/\mathrm{Mpc}$ for $z = 1.5$.

It is convenient to express the $P^{(s)}(k,\mu)$ power spectrum as an expansion in the Legendre polynomial basis, $P^{(\ell)}$, defined as,

$$P_h^{(\ell)}(k) = (2\ell+1)\int_0^1 d\mu\, P_h^{(s)}(k,\mu)L_\ell(\mu), \tag{2.15}$$

where $L_\ell$ are the Legendre polynomials of order $\ell$. The first non-vanishing $P^{(\ell)}$ are the monopole ($\ell = 0$), quadrupole ($\ell = 2$) and hexadecapole ($\ell = 4$),

$$P_h^{(0)} \;=\; P^{\mathrm{lin}}(k)\left(b_1^2 + \frac{2}{3}fb_1 + \frac{1}{5}f^2\right) \tag{2.16}$$

$$P_h^{(2)} \;=\; P^{\mathrm{lin}}(k)\left(\frac{4}{3}fb_1 + \frac{4}{5}f^2\right) \tag{2.17}$$

$$P_h^{(4)} \;=\; P^{\mathrm{lin}}(k)\left(\frac{8}{35}f^2\right). \tag{2.18}$$

In this paper we only focus on the monopole and quadrupole, as the hexadecapole has low signal-to-noise.

### 2.2 Halo bispectrum

The halo bispectrum of the density field, can be written according to Eq. 2.6 as,

$$B_{\rm h}(\mathbf{k}_1,\mathbf{k}_2) = b_1^3 B_\delta(\mathbf{k}_1,\mathbf{k}_2) + b_1^2\left[b_2 P_{\delta\delta}(k_1)P_{\delta\delta}(k_2) + b_{s^2}P_{\delta\delta}(k_1)P_{\delta\delta}(k_2)S_2(\mathbf{k}_1,\mathbf{k}_2) + \text{cyc.}\right]$$

where we have neglected terms proportional to $b_2^2$ and $b_{s^2}^2$, which are of higher-order. We consider that none of these terms can be renormalised in such a way that they contribute on large scales, as we did for $b_{3\rm nl}$ in the power spectrum, and neglect them to leading order. Applying the tree-level prediction for the dark matter bispectrum we write the halo bispectrum as a function of the matter power spectrum,

$$\begin{aligned} B_{\rm h}(\mathbf{k}_1,\mathbf{k}_2) \;=\; & b_1^3 P_{\delta\delta}(k_1)P_{\delta\delta}(k_2)2F_2(\mathbf{k}_1,\mathbf{k}_2) + b_1^2 b_2 P_{\delta\delta}(k_1)P_{\delta\delta}(k_2) + \\ & + b_1^2 b_{s^2} P_{\delta\delta}(k_1)P_{\delta\delta}(k_2)S_2(\mathbf{k}_1,\mathbf{k}_2) + \text{cyc.}, \end{aligned} \tag{2.19}$$

where $F_2$ is given by the second order kernel in standard perturbation theory (SPT) [37],

$$F_2(\mathbf{k}_i,\mathbf{k}_j) = \frac{5}{7} + \frac{1}{2}\cos(\alpha_{ij})\left(\frac{k_i}{k_j}+\frac{k_j}{k_i}\right) + \frac{2}{7}\cos^2(\alpha_{ij}), \tag{2.20}$$

where $\alpha_{ij}$ is the angle between the vectors $\mathbf{k}_i$ and $\mathbf{k}_j$. It was shown that substituting the $F_2$ kernel by an effective kernel, namely $F_2^{\rm eff}$, the dark matter bispectrum description can be extended to mildly non-linear scales with respect to the tree-level prediction [1, 38],

$$\begin{aligned} F_2^{\rm eff}(\mathbf{k}_i,\mathbf{k}_j) \;=\; & \frac{5}{7}a(n_i,k_i,\mathbf{a}^F)a(n_j,k_j,\mathbf{a}^F) + \frac{1}{2}\cos(\alpha_{ij})\left(\frac{k_i}{k_j}+\frac{k_j}{k_i}\right)b(n_i,k_i,\mathbf{a}^F)b(n_j,k_j,\mathbf{a}^F) \\ & + \frac{2}{7}\cos^2(\alpha_{ij})c(n_i,k_i,\mathbf{a}^F)c(n_j,k_j,\mathbf{a}^F), \end{aligned} \tag{2.21}$$

where the definition of the $a$, $b$ and $c$ functions can be found in [1]. The set of $\mathbf{a}^F \equiv \{a_1^F, a_2^F, \ldots, a_9^F\}$ parameters is a empirical fit to N-body data,

$$\begin{aligned} a_1^F &= 0.484 \quad & a_4^F &= 0.392 \quad & a_7^F &= 0.128 \\ a_2^F &= 3.740 \quad & a_5^F &= 1.013 \quad & a_8^F &= -0.722 \\ a_3^F &= -0.849 \quad & a_6^F &= -0.575 \quad & a_9^F &= -0.926\,. \end{aligned}$$

This set of parameters does not depend on redshift and is assumed to be weakly dependent on cosmology. Since the dependence of the $F_2$ kernel with cosmology is assumed weak [39], we expect the dependence of $\mathbf{a}^F$ to be weak as well. We demonstrated the validity of this assumption in Appendix B of [1].

To describe the halo bispectrum in redshift space on large scales, one can apply the standard perturbation theory formalism. In this case, the form of the bispectrum formula is the same as that in Eq. 2.19, but substituting the kernels by new redshift space ones [40–43],

$$B_{\rm h}^{(s)}(\mathbf{k}_1,\mathbf{k}_2) = D_{\rm fog}^B(k_1,k_2,k_3,\sigma_{\rm fog}^B)\left[2P_{\delta\delta}(k_1)\,Z_1(\mathbf{k}_1)\,P_{\delta\delta}(k_2)\,Z_1(\mathbf{k}_2)\,Z_2(\mathbf{k}_1,\mathbf{k}_2) + \text{cyc.}\right] \tag{2.22}$$

where $Z_i$ are the redshift space kernels, in tree-level perturbation theory they are,

$$Z_1(\mathbf{k}_i) \equiv (b_1 + f\mu_i^2) \tag{2.23}$$

$$\begin{aligned} Z_2(\mathbf{k}_1,\mathbf{k}_2) \equiv\; & b_1\left[F_2(\mathbf{k}_1,\mathbf{k}_2) + \frac{f\mu k}{2}\left(\frac{\mu_1}{k_1}+\frac{\mu_2}{k_2}\right)\right] + f\mu^2 G_2(\mathbf{k}_1,\mathbf{k}_2) + \\ & + \frac{f^3\mu k}{2}\mu_1\mu_2\left(\frac{\mu_2}{k_1}+\frac{\mu_1}{k_2}\right) + \frac{b_2}{2} + \frac{b_{s^2}}{2}S_2(\mathbf{k}_1,\mathbf{k}_2), \end{aligned} \tag{2.24}$$

and $\mu \equiv (\mu_1 k_1 + \mu_2 k_2)/k$, $k^2 = (\mathbf{k}_1 + \mathbf{k}_2)^2$. $F_2$ and $G_2$ are the second-order real-space kernels of the densities and velocities respectively [37],

$$G_2(\mathbf{k}_i, \mathbf{k}_j) = \frac{3}{7} + \frac{1}{2}\cos(\alpha_{ij})\left(\frac{k_i}{k_j} + \frac{k_j}{k_i}\right) + \frac{4}{7}\cos^2(\alpha_{ij}). \tag{2.25}$$

Below we will modify this expression to push further into the non-linear regime. $D^B_{\rm fog}$ stands for the Fingers-of-God (FoG) damping term due to the intra-halo velocity dispersion, analogously to Eq 2.14. In this paper we assume that it is described by [40],

$$D^B_{\rm fog}(k_1, k_2, k_3, \sigma^B_{\rm FoG}[z]) \;=\; \left(1 + [k_1^2\mu_1^2 + k_2^2\mu_2^2 + k_3^2\mu_3^2]^2\sigma^B_{\rm FoG}[z]^2/2\right)^{-2}, \tag{2.26}$$

where $\sigma^B_{\rm fog}(z) \equiv \sigma^B_0(z) f(z) D(z)$. In this paper we consider $\sigma^P_0$ and $\sigma^B_0$ to be independent parameters having different roles, with $\sigma^P_0$ acting as a general non-linear damping term while $\sigma^B_0$ only corrects for the FoG. Note that when $f \to 0$, then $Z_1 \to b_1$ and $Z_2 \to b_1 F_2 + b_2/2 + b_{s^2}/2 S_2$, and the real space prediction is recovered.

As for the power spectrum, we can decompose the redshift space bispectrum in Legendre basis. In particular the monopole is,

$$B^{(0)}_{\rm h}(k_1, k_2, k_3) = \int d\mu_1 d\mu_2 B^{(s)}_{\rm h}(\mathbf{k}_1, \mathbf{k}_2) = \int_{-1}^{+1} d\mu_1 \int_0^{2\pi} d\varphi\, B^{(s)}_{\rm h}(\mathbf{k}_1, \mathbf{k}_2) \tag{2.27}$$

where $\varphi$ has been defined to satisfy, $\mu_2 \equiv \mu_1 x_{12} - \sqrt{1-\mu_2^2}\sqrt{1-x_{12}^2}\cos\varphi$, with $x_{12} \equiv (\mathbf{k}_1 \cdot \mathbf{k}_2)/(k_1 k_2)$.

The expression for the halo bispectrum monopole can be analytically written in the absence of FoG term ($D^B_{\rm fog} = 1$) as,

$$\begin{aligned} B^{(0)}_{\rm h}(\mathbf{k}_1, \mathbf{k}_2) \;=\; & P_{\delta\delta}(k_1) P_{\delta\delta}(k_2) b_1^4 \left\{ \frac{1}{b_1} F_2(\mathbf{k}_1, \mathbf{k}_2) \mathcal{D}^{(0)}_{\rm SQ1} + \frac{1}{b_1} G_2(\mathbf{k}_1, \mathbf{k}_2) \mathcal{D}^{(0)}_{\rm SQ2} \right. \\ & \left. + \left[\frac{b_2}{b_1^2} + \frac{b_{s^2}}{b_1^2} S_2(\mathbf{k}_1, \mathbf{k}_2)\right] \mathcal{D}^{(0)}_{\rm NLB} + \mathcal{D}^{(0)}_{\rm FoG} \right\} + \text{cyc.} \end{aligned} \tag{2.28}$$

where the $\mathcal{D}$-terms are defined in [40].

### 2.3 Halo shot noise

We use a simple model for the halo shot noise parametrised by 1 free-parameter, $A_{\rm noise}$ that extends the standard Poisson noise model,

$$P_{\rm noise} \;=\; (1 - A_{\rm noise}) P_{\rm Poisson}, \tag{2.29}$$

$$B_{\rm noise}(k_1, k_2, k_3) \;=\; (1 - A_{\rm noise}) B_{\rm Poisson}(k_1, k_2, k_3). \tag{2.30}$$

We fit $A_{\rm noise}$ assuming a uniform prior between -1 and +1. Beyond these limits a more complex modelling would be needed. Note that $A_{\rm noise} = 0$ corresponds to the pure Poisson shot noise, whereas $A_{\rm noise} < 0$ produces a super-Poisson shot noise, and $A_{\rm noise} > 0$ a sub-Poisson shot noise. In principle sub-Poisson shot noise is related to halo exclusion whereas super-Poisson shot noise to particle clustering. Consequently, $A_{\rm noise}$ is probably scale-dependent. However for simplicity we assume that for the range of scales studied here, $0.01 \leq k_i\,[h/\text{Mpc}] \leq 0.25$, this parameter is constant.

### 2.4 Parameter estimation

We are interested in estimating a set of parameters, $\mathbf{\Psi}$, from the power spectrum and bispectrum. $\mathbf{\Psi}$ includes cosmologically interesting parameters such as the bias parameters, the amplitude of the matter power spectrum $\sigma_8$ and the logarithmic growth factor parameter $f$, as well as nuisance parameters, such as shot noise parameters and the damping factors of the FoG terms. We do not allow the spectral index, $n_s$, the Hubble parameter $h$ and the matter and baryon densities, $\Omega_m$ and $\Omega_b$ to vary

from their fiducial values, thus assuming a fixed shape of the dark matter linear power spectrum. We refer to these parameters as $\mathbf{\Omega}$.

In principle the optimal way to analyse a statistical quantity is to model its probability density function and proceed to parameter fitting from there. However, the probability distribution for the bispectrum especially in the mildly non-linear regime is not known (although some progress are being made see e.g., [44]); even if one invokes the central limit theorem and models the distribution of bispectrum modes as a multi-variate Gaussian, the evaluation of its covariance would be challenging (see e.g., eq. 38-42 of [45], appendix A of [41] and discussion above). In addition we want to analyse jointly power spectrum and bispectrum whose joint distribution is not known. Another approach is therefore needed. In order to estimate the set of $\mathbf{\Psi}$ parameters, we opt for the approach proposed in [46], which consists of introducing a suboptimal but unbiased estimator. Thus, following this formalism, we define the $\chi^2_{\rm diag.}$-function as,

$$\chi^2_{\rm diag.}(\mathbf{\Psi}) = \sum_{k-{\rm bins}} \frac{\left[P^{\rm meas.}_{(i)}(k) - P^{\rm model}(k,\mathbf{\Psi};\mathbf{\Omega})\right]^2}{\sigma_P(k)^2} + \\ + \sum_{\rm triangles} \frac{\left[B^{\rm meas.}_{(i)}(k_1,k_2,k_3) - B^{\rm model}(k_1,k_2,k_3,\mathbf{\Psi};\mathbf{\Omega})\right]^2}{\sigma_B(k_1,k_2,k_3)^2}, \tag{2.31}$$

where $\sigma_P$ and $\sigma_B$ are the diagonal terms of the covariance matrix for the power spectrum and bispectrum respectively. Therefore, Eq. 2.31 ignores the contribution from off-diagonal terms, and takes into account only the diagonal terms. In this paper, the terms $\sigma_P$ and $\sigma_B$ are computed from the dispersion of the different realizations of dark matter or halo population. By ignoring the off diagonal terms of the covariance matrix in the $\chi^2_{\rm diag.}$ definition we do not have a have maximum likelihood estimator which is minimum variance, optimal and unbiased. This estimator is sub-optimal but unbiased. We have checked (and we will show it explicitly in § 7.1) that this estimator is indeed unbiased. Furthermore, *a)* the particular value of the $\chi^2_{\rm diag.}$ at its minimum is meaningless and should not be used to estimate a goodness of fit and *b)* the errors on the parameters cannot be estimated by standard $\chi^2_{\rm diag.}$ differences.

We use a Nelder-Mead based-method of minimization [47] to a set of best-fitting parameters that minimize $\chi^2_{\rm diag.}$ for each realisation $i$, namely $\mathbf{\Psi}_{(i)}$.

Therefore, the main point of this method is that $\langle\mathbf{\Psi}_{(i)}\rangle$ is an unbiased estimator of the true set $\mathbf{\Psi}_{\rm true}$ and that the dispersion of $\mathbf{\Psi}_{(i)}$ is a suitable estimator of the error: $\mathbf{\Psi}_{\rm true} \simeq \langle\mathbf{\Psi}_{\rm i}\rangle \pm \sqrt{\langle\mathbf{\Psi}^2_{\rm i}\rangle - \langle\mathbf{\Psi}_{\rm i}\rangle^2}$. This procedure will be applied in § 6 and § 7, using the total amount of realizations (60 for dark matter and 20 for haloes) in order to obtain $\mathbf{\Psi}$ and their errors.

## 3 Simulations

The simulations used in this paper consists of two different sets, one providing dark matter fields and halo catalogues. These simulations have been used in previous works (see [1] for dark matter and [48] for the halo catalogue).

### 3.1 Dark matter particles simulations

The dark matter particle set of simulations consists of N-body dark matter only simulations with flat LCDM cosmology listed in Table 1 as "Sim DM". The box size is $L_b = 2.4\,{\rm Gpc}/h$ with periodic boundary conditions and the number of particles is $N_p = 768^3$ with 60 independent runs. The initial conditions were generated at $z = 49$ by displacing the particles according to the second-order Lagrangian PT from their initial grid points. The initial power spectrum of the density fluctuations was computed by CAMB [49]. Taking only the gravitational interaction into account, the simulation was performed with GADGET-2 code [50]. There are four snapshots at redshifts $z = 0$, $z = 0.5$, $z = 1.0$ and $z = 1.5$. In order to obtain the dark matter field from particles we apply the Cloud-in-Cell (CiC) prescription using $512^3$ grid cells. Thus the size of the grid cells is 4.68 Mpc/$h$.

### 3.2 Dark matter halo catalogue

The dark matter halo catalogue set is based on N-body dark matter particles simulations with the cosmology listed in Table 1 as "Sim HC". The box size is $L_b = 1.5\,\mathrm{Gpc}/h$. The original mass of the dark matter particles is $m_p = 7.6 \times 10^{10}\,M_\odot/h$, and the minimum halo mass has been selected to be $7.8 \times 10^{12}\,M_\odot/h$. The halo catalogues are generated by the Friends-of-Friends algorithm by [51] with a linking length of 0.168 times the mean inter-particle spacing. There is one snapshot at $z = 0.55$. In order to extract the halo field, a CiC prescription is also used with $512^3$ grid cells, whose size is $2.93\,\mathrm{Mpc}/h$.

| | $\Omega_\Lambda$ | $\Omega_m$ | $h$ | $\Omega_b h^2$ | $n_s$ | $\sigma_8$ | $z$ | $L_b$[Gpc/$h$] | $V_{\rm eff}$ [Gpc/h]$^3$ |
|---|---|---|---|---|---|---|---|---|---|
| Sim DM | 0.73 | 0.27 | 0.7 | 0.023 | 0.95 | 0.79 | 0 - 1.5 | 2.4 | $13.824 \times 60$ |
| Sim HC | 0.726 | 0.274 | 0.7 | 0.0224 | 0.95 | 0.8 | 0.55 | 1.5 | $3.375 \times 20$ |

**Table 1**. Cosmological parameter of the two sets of simulations used in this paper: dark matter only (DM) and halo catalogs (HC). Several cosmological parameters are listed: the dark energy density, $\Omega_\Lambda$, matter density $\Omega_m$, Hubble parameter $h$, physical baryon density $\Omega_b h^2$, primordial power-law power spectrum spectral index $n_s$ and amplitude of the primordial power spectrum linearly extrapolated at $z = 0$ $\sigma_8$. Also the box size of the simulation is provided, $L_b$, and the effective volume per realization times the total number of realizations, $V_{\rm eff}$.

## 4 Dark matter power spectrum multipoles

We start by illustrating the ability of the theoretical modelling to describe the real-space dark matter power spectrum as well as its redshift space multipoles. We use the TNS model in combination with the 2LRPT model (hereafter TNS-2LRPT) to describe the power spectrum multipoles.

The description of the dark matter power spectrum in redshift space requires the parameter $\sigma_0^P$, as in Eq. 2.14. Although there are some prescriptions to approximate this parameter analytically (if it were only correcting for the FoG), in this paper we treat it as a nuisance parameter to be fit from N-body simulations measurements of the monopole and quadrupole. We assume that this parameter can in principle change freely with redshift but not with the scale. In Fig. 1 we show its best-fitting values as a function of the maximum scale used, for different redshift snapshots: $z = 0$ (red solid line), $z = 0.5$ (blue solid line), $z = 1.0$ (green solid line) and $z = 1.5$ (orange solid line). The dashed lines show the $\sigma_0^P$ value for the smallest scale (largest $k$) we trust the model, namely $k_c$. This scale is defined as the largest that satisfies, $|P_{\rm sim}/P_{\rm model}| < 1.02$ for the real space power spectrum. The value for $\sigma_0^P(k_{\rm max} = k_c)$ as well as the $k_c$ scale, are shown in Table 2 for the four redshift snapshots studied here. Note that in Fig. 1, the best-fitting $\sigma_0^P$ value is only plotted for $k_{\rm max} \leq k_c$.

| $z$ | 0 | 0.5 | 1.0 | 1.5 |
|---|---|---|---|---|
| $\sigma_0^P(z)$ [Mpc/$h$] | 7.8 | 7.0 | 6.2 | 5.6 |
| $D(z)$ | 1.000 | 0.782 | 0.623 | 0.511 |
| $f(z)$ | 0.483 | 0.723 | 0.852 | 0.915 |
| $k_{\rm c}(z)$ [$h$/Mpc] | 0.11 | 0.16 | 0.22 | $> 0.25$ |

**Table 2**. Best fitting values of $\sigma_0^P$ from the dark matter power spectrum monopole and quadrupole measurements at different $z$. The growth factor parameters $D$ and $f$, as well as the $k_{\rm c}$ values are also reported.

From the values of Table 2, we observe that the best-fitting $\sigma_0^P(z)$ depends on redshift: lower redshift snapshots present a more severe damping at a given scale and therefore $\sigma_0^P$ decreases with $z$. We observe a similar behaviour for the quantity $\sigma_0^P(z)D(z)f(z)$. However, the quantity $\sigma_0^P(z)f(z)$ presents a weak redshift-dependence for $z = 0.5$, 1.0 and 1.5, although at $z = 0$ has a significantly different value.

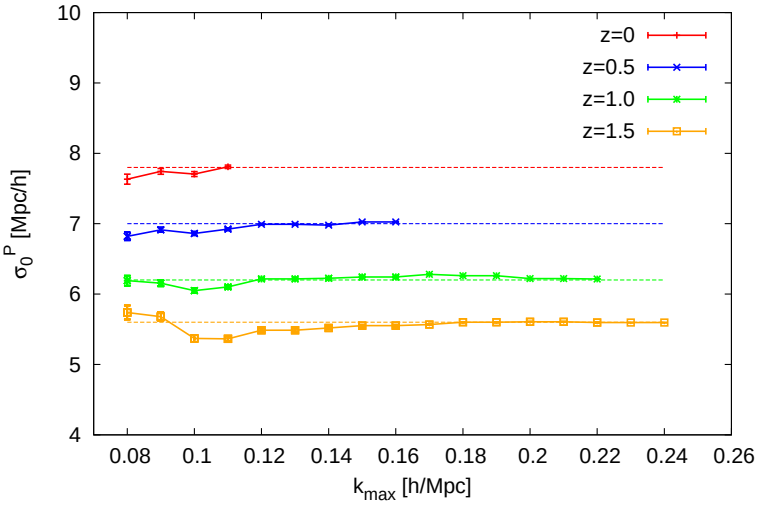


**Figure 1**. Best-fitting power spectrum FoG parameter, $\sigma_0$ as a function of $k_{\rm max}$ (solid lines). The colour notation correspond to the redshift snapshot: $z = 0$ (red), $z = 0.5$ (blue), $z = 1.0$ (green) and $z = 1.5$ (orange) as indicated in the key. Dashed lines show the value at $k_c$, which is given in Table 2. Note that we only plot the best-fitting value up to $k_c(z)$ (scale at which the real space modelling fails at more than 2% level).

Fig. 2 presents the dark matter power spectrum in real space (top panels), the dark matter redshift space monopole (middle panel) and quadrupole (bottom panels) for $z = 0$ (left panels) and $z = 1$ (right panels). In the top sub-panels the power spectrum (normalised to a non-wiggle model) is displayed for N-body measurements (black symbols with error-bars). Solid lines correspond to the theoretical predictions of the TNS model (with $b_1 = 1$ and $b_2 = b_{s^2} = b_{3\rm nl} = 0$) implemented with 2LRPT: red for the real space power spectrum, blue for the redshift space monopole and green for the quadrupole. For the monopole and quadrupole the values of $\sigma_0^P(k_c)$ listed in Table 2 have been used. The growth factors $f$ and $D$ (listed also in Table 2) have been fixed at their true values. The errors-bars correspond to the error on the mean of 60 realizations, for a total effective volume of $V_{\rm eff} \simeq 829\,[{\rm Gpc}/h]^3$.

From Fig. 2 we see that the TNS model in combination with 2LRPT model is able to describe the two-point N-body statistics with an accuracy of $\sim 1\%$ for the real space power spectrum and redshift space monopole up to $k_c$. The quadrupole is described typically with $\sim 2\%$ accuracy.

In conclusion, the TNS model in combination with the 2LRPT model is able to describe with per-cent accuracy the two-points real space statistics for dark matter particles without any free parameters. The main two-point redshift space statistics, the monopole and the quadrupole, are described with per-cent precision as well and require one free parameter per redshift snapshot. The function of this parameter is to reduce an excess of power at small scales, typically produced by non-linear processes such as intra-halo velocity dispersion.

## 5 Dark matter bispectrum modelling in redshift space

The main goal of this paper is to provide a modification of the SPT model prediction for the bispectrum in redshift space given by Eq. 2.22 for dark matter and by Eq 2.28 for haloes. Typically the SPT approach works well at large scales and at high redshifts, but breaks down in the mildly non-linear regime.

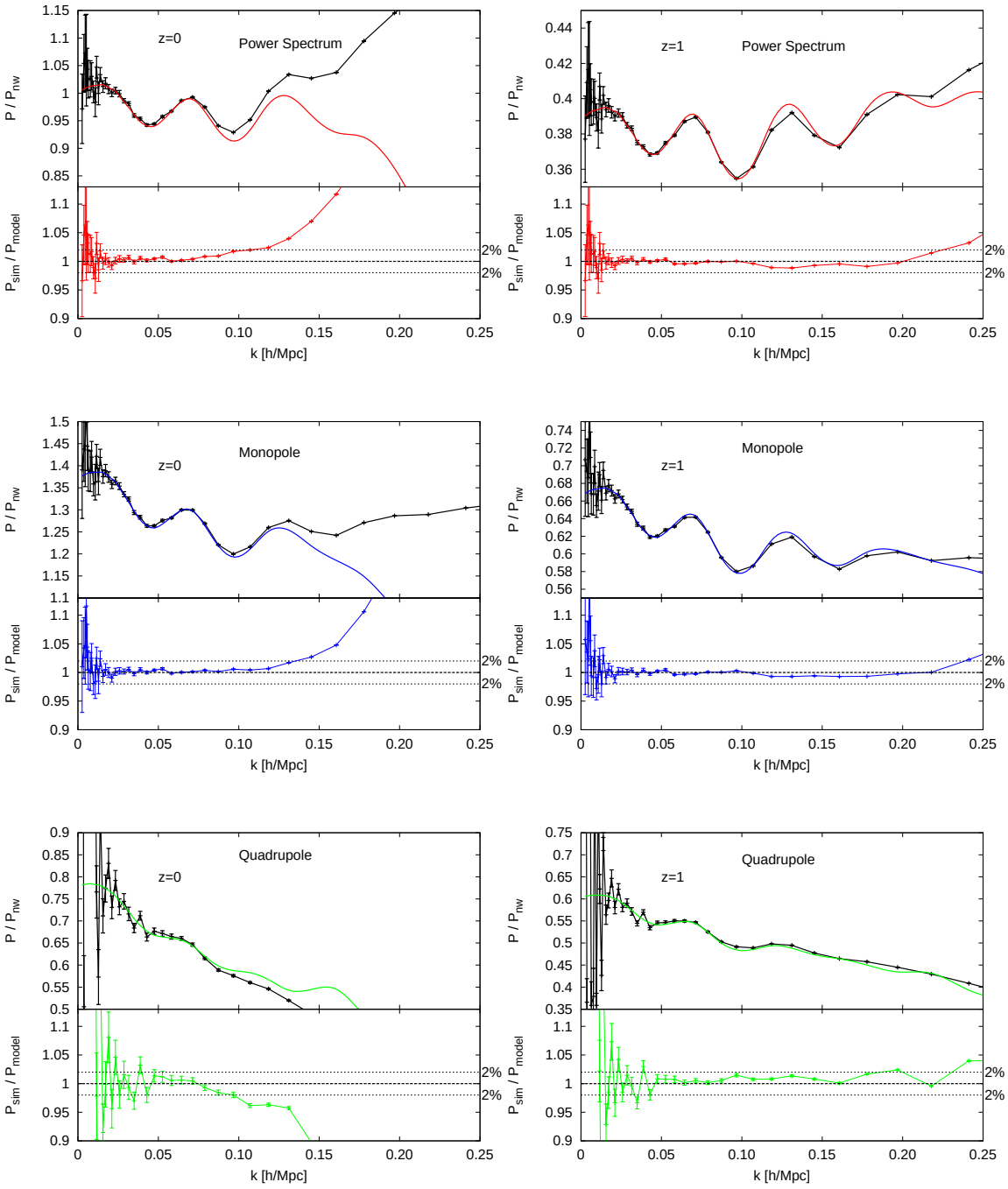


**Figure 2**. Power spectra in real space (top panels), monopoles (middle panels) and quadrupoles (bottom panels), for $z = 0$ (left panels) and $z = 1$ (right panels). Black symbols are measurements from 60 N-body dark mater simulations, whereas color lines are predictions for dark matter using the TNS model in combination with 2LRPT model with $\sigma^P_{\rm fog}$ as a free parameter. The top-subpanels show the power spectrum normalized by a non-wiggle linear model and the bottom sub-panels show the relative deviation of the N-body dark matter measurements to the corresponding models. The values for $\sigma^P_{\rm fog}$ used in the models are listed in Table 2.

We follow a similar procedure to that in [1]. It consist of modifying the SPT kernels into effective kernels with free parameters to be fitted from N-body simulations. In this case we change the velocity kernel $G_2$ of Eq. 2.24 by an effective kernel of the form,

$$G_2^{\rm eff}(\mathbf{k}_i,\mathbf{k}_j) = \frac{5}{7}a(n_i,k_i,\mathbf{a}^G)a(n_j,k_j,\mathbf{a}^G) + \frac{1}{2}\cos(\alpha_{ij})\left(\frac{k_i}{k_j}+\frac{k_j}{k_i}\right)b(n_i,k_i,\mathbf{a}^G)b(n_j,k_j,\mathbf{a}^G) \quad (5.1)$$
$$+ \frac{2}{7}\cos^2(\alpha_{ij})c(n_i,k_i,\mathbf{a}^G)c(n_j,k_j,\mathbf{a}^G),$$

where the functions $a$, $b$ and $c$ are the same as used in $F_2^{\rm eff}$ and can be found in [1]. We assume that the set of parameters $\mathbf{a}^G \equiv \{a_1^G, a_2^G, \ldots, a_9^G\}$, is redshift-, scale- and shape-independent, and needs to be fitted from the measurement of the redshift space bispectrum monopole in N-body simulations. We consider the damping terms of Eq. 2.26 to describe the FoG features of the bispectrum. We allow this parameter to depend on the redshift and to be independent of the $\sigma_0^P$ of Table 2.

We consider different approaches to describe the redshift space bispectrum monopole. All of them are based on SPT leading order correction (Eq. 2.22) with different changes in the definition of the redshift space kernels,

1. **SPT approach**. We use the SPT prediction of Eq. 2.22 with the SPT kernels $F_2$ and $G_2$ of Eqs. 2.20 and 2.25. We include the FoG effect through the damping functions of Eq. 2.26. This function contains one free parameter, $\sigma_0^B$. We allow this parameter to freely vary with redshift, but we consider it scale- and shape-independent. Hence, this approach has four-free parameters for the whole redshift range. Hereafter we refer the bispectrum prediction of this model as $B^{\rm spt}$.

2. **Hybrid approach**. We use the prediction of Eq. 2.22 taking the effective kernel $F_2^{\rm eff}$ from Eq. 2.21 instead of the SPT form of $F_2$. The $\mathbf{a}^F$ values from [1] are used. We consider the SPT kernel for $G_2$. As for the SPT approach, we use Eq. 2.26 to describe the FoG effect. We refer to the bispectrum prediction from this model as $B^F$.

3. **Effective approach**. We use the Eq. 2.22 structure with the effective kernel $F_2^{\rm eff}$ of Eq. 2.21, and the effective $G_2^{\rm eff}$ kernel from Eq. 5.1 with a set of nine free parameters, $\mathbf{a}^G$, to be fitted. We add the FoG-term of Eq. 2.26 with one extra free parameter per redshift snapshot. We will refer to this model as $B^{\rm FG}$.

We use the method described in § 2.4 for estimating $\mathbf{a}^G$, fixing the bias parameters, $f$ and $\sigma_8$ to their true values. There are a large number of possible triangular shapes to consider and is not practical to consider them all. However, is not necessary to compute all possible triplets as their bispectra are highly correlated. Therefore, here we consider only triangles with $k_2/k_1 = 1.0$, 1.5, 2.0 and 2.5. We estimate that $\sim 80\%$ of the full information of the bispectrum is contained by these shapes at $k \sim 0.1\,h$/Mpc. Since we expect that the theory breaks down at different scales at different $z$ we set the fitting range to: $k_i \leq 0.15\,h$/Mpc for $z = 0$, $k_i \leq 0.18\,h$/Mpc for $z = 0.5$, $k_i \leq 0.21\,h$/Mpc for $z = 1.0$ and $k_i \leq 0.25\,h$/Mpc for $z = 1.5$. We have checked iteratively that these are the maximum scales that the **Effective approach** can describe with $\lesssim 5\%$ accuracy. The set of best-fitting $\mathbf{a}^G$ parameters are,

$$\begin{array}{lll} a_1^G = 3.599 & a_4^G = -3.588 & a_7^G = 5.022 \\ a_2^G = -3.879 & a_5^G = 0.336 & a_8^G = -3.104 \\ a_3^G = 0.518 & a_6^G = 7.431 & a_9^G = -0.484\,. \end{array}$$

The fitting process also provides best-fitting values for $\sigma_0^B$. These values are listed in Table 3 for the different models used. The $\sigma_0^P$ parameters found in § 4 are also shown for reference. Note that we expect that the $\sigma_0^P$ and $\sigma_0^B$ parameters change as a function of the selected tracer as well as function of redshift. However, the $\mathbf{a}^G$ set (as well as $\mathbf{a}^F$) is assumed to be universal.

We are aware that this result may depend on the cosmology. However, as we have mentioned for the $\mathbf{a}^F$ fit, the dependence of the $F_2$ and $G_2$ kernels on cosmology is very weak, so this holds also for

| $z$ | 0 | 0.5 | 1.0 | 1.5 |
|---|---|---|---|---|
| $\sigma_0^B(B^{\rm spt})$ | 43. | 33.7 | 25.0 | 20.3 |
| $\sigma_0^B(B^F)$ | 51.93 | 38.5 | 28.28 | 23.56 |
| $\sigma_0^B(B^{FG})$ | 41.67 | 26.9 | 17.4 | 11.67 |
| $\sigma_0^P$ | 7.8 | 7.0 | 6.2 | 5.6 |

**Table 3**. Best-fitting values for $\sigma_0^B(z)$ (in Mpc/$h$) for different bispectrum models for dark matter (see text for details). These values correspond to the different models shown in Figs. 3 - 6. In the last row for comparison we also show the values for $\sigma_{\rm fog}^P$ from the monopole-to-quadrupole ratio.

the $\mathbf{a}^F$ and $\mathbf{a}^G$ parameters. Furthermore, since we have performed the fit for a wide range of redshifts, any cosmology dependence that is equivalent to a redshift re-scaling can be described by the model.

In Figs. 3- 6 we compare the three approaches, $B^{\rm spt}$ (green lines), $B^{\rm F}$ (blue lines), $B^{\rm FG}$ (red lines), with the N-body dark matter monopole bispectrum (black symbols) for $z = 0$, 0.5, 1.0, 1.5 respectively. The error-bars correspond to the error on the mean of 60 realizations, with a total volume of $V_{\rm eff} \simeq 829\,[{\rm Gpc}/h]^3$. In the top sub-panels the redshift-space bispectrum monopole is shown. For visualisation reasons this quantity has been normalised by the measurement of the bispectrum in real space. In the lower sub-panel we plot the percentile deviation between the model and the measured bispectrum.

The accuracy of the different models depends noticeably on the $k$-range, redshift and triangular shapes we are considering. As a general trend, we observe that at large scales and high redshifts the three models studied here do not show large differences and describe well the N-body measurements. This makes sense, since in the large scale limit, $F_2^{\rm eff} \to F_2$, and $G_2^{\rm eff} \to G_2$. On the other hand, at low redshift and small scales the three models present different predictions. Typically, $B^{FG}$ best describes the N-body data, followed first by $B^F$ and finally by $B^{\rm spt}$. This is the expected behaviour, given the number of free parameters and complexity of each model.

For $B^{FG}$, at $z = 0$ we see that the differences between the model and the N-body predictions are $\leq 10\%$ when $k_i \leq 0.15\,h/{\rm Mpc}$, and $\lesssim 5\%$ when $k_i \leq 0.10\,h/{\rm Mpc}$. For $z = 0.5$, the agreement between $B^{FG}$ and N-body simulations is $\leq 10\%$ when $k_i \leq 0.20\,h/{\rm Mpc}$ and $\lesssim 5\%$ when $k_i \leq 0.15\,h/{\rm Mpc}$. For $z = 1.0$ we observe that for the whole range studied here, $k \leq 0.25\,h/{\rm Mpc}$, we always have an accuracy of $\leq 10\%$, whereas when we restrict it to $k_i \leq 0.17\,h/{\rm Mpc}$, the accuracy increases to $\lesssim 5\%$. Finally for $z = 1.5$ we observe that the accuracy is $\lesssim 5\%$ for $k \leq 0.20\,h/{\rm Mpc}$.

In Table 3 we report the best-fitting values of $\sigma_0^B$, for the different models used, and for the different redshifts. We note that, for each redshift, the value of $\sigma_0^B$ depends strongly on the model. In particular, $B^{FG}$ requires a smaller $\sigma_0^B$ for describing the bispectrum than the other two models. A possible explanation for this behaviour, is that for $B^{\rm spt}$ and $B^F$ this parameter absorbs higher levels of systematic imperfections of the modeling than for $B^{FG}$. Based on this, we expect that when we use $B^{FG}$ to model the halo bispectrum, setting $D_{\rm fog}^B$ to 1, will produce a good estimate for the halo bispectrum, since $D_{\rm fog}^B$ was correcting only for the FoG and not for any other systematic effects. We study this in detail in § 6. We also note that the ratio between $\sigma_0^P$ and $\sigma_0^B$ for any of the models is not constant as a function of $z$.

In the next section, we apply model $B^{FG}$ with the fitted $\mathbf{a}^G$ parameters to describe the monopole bispectrum of haloes with a similar cosmology to the one used in this section.

## 6 Extension to biased tracers

In this section we aim to show how the $B^{FG}$ model can be used to describe the bispectrum of N-body haloes. We use a slightly different cosmological model than used in the previous section to fit the values of $\mathbf{a}^G$. The main purpose of this is to show that the $\mathbf{a}^G$ found in last section do not depend on the FoG feature, and that $B^{FG}$ is suitable to be applied to any dark matter tracer and therefore suitable to be applied to galaxy surveys. We also compare $B^{FG}$ with the predictions of model $B^{\rm spt}$ to see the improvement.

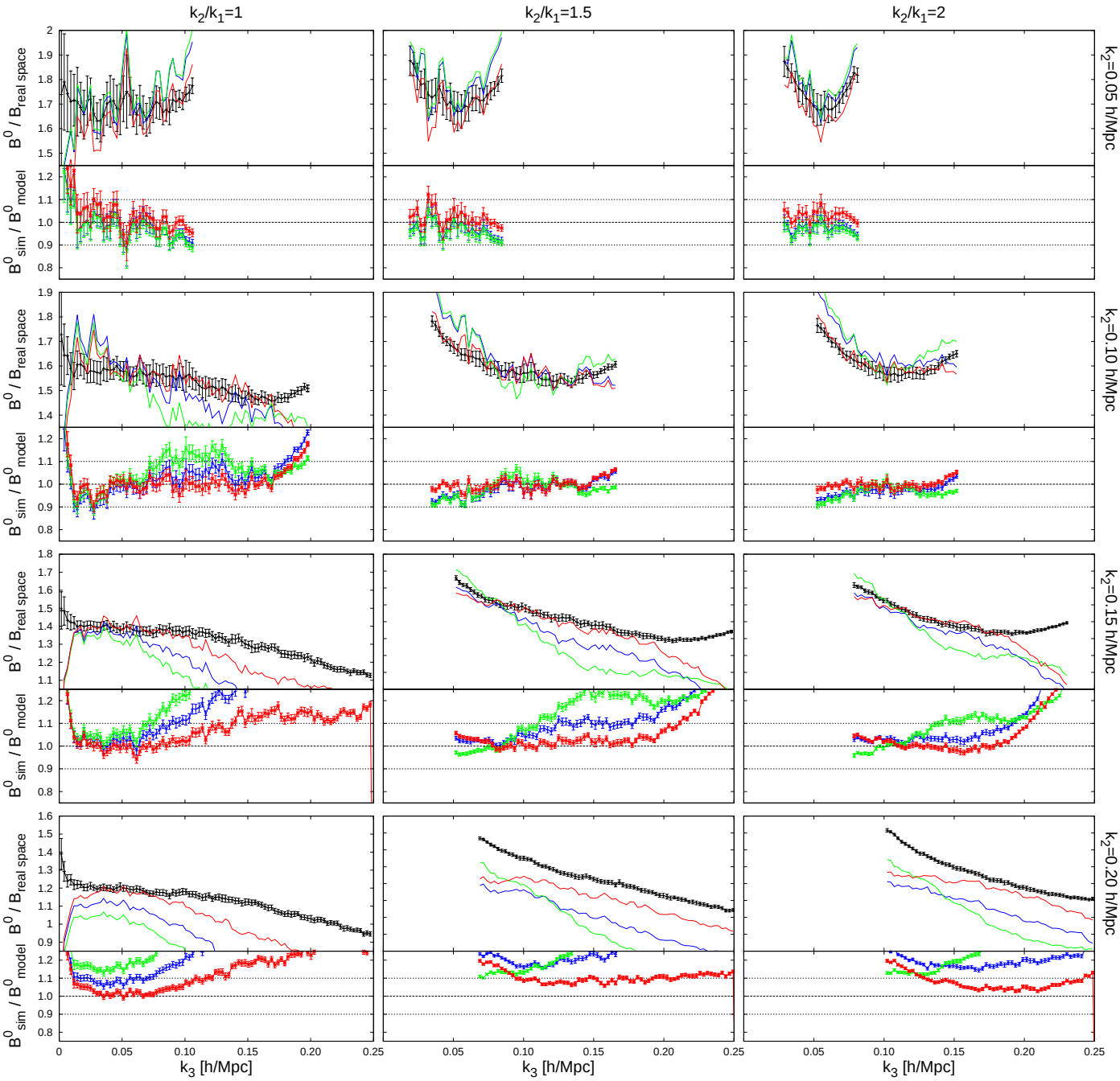


**Figure 3**. Top sub-panels: dark matter monopole bispectrum normalised to the real space matter bispectrum for different triangle configurations. First column, second and third column panels are triangles with $k_2/k_1 =$ 1.0, 1.5 and 2 respectively. Different rows show different scales: first, second, third and forth rows correspond to $k_2 = 0.05$, 0.10, 0.15 and 0.20 $h$/Mpc as indicated. Black symbols correspond to N-body simulations whereas colour lines to the different models based on Eq. 2.22: $B^{\rm spt}$ (green lines), $B^{\rm F}$ (blue line) and $B^{\rm FG}$ (red) (see text for description). Bottom sub-panels: relative deviation of each of these models to the dark matter measurement. All panels are at $z = 0$.

In order to describe the halo biasing, we use the non-local and non-linear bias model presented in Eq. 2.6. Since we are dealing with haloes, we cannot ignore the contribution of shot noise. Due to halo exclusion and clustering we expect some deviations from the Poisson noise prediction. In order

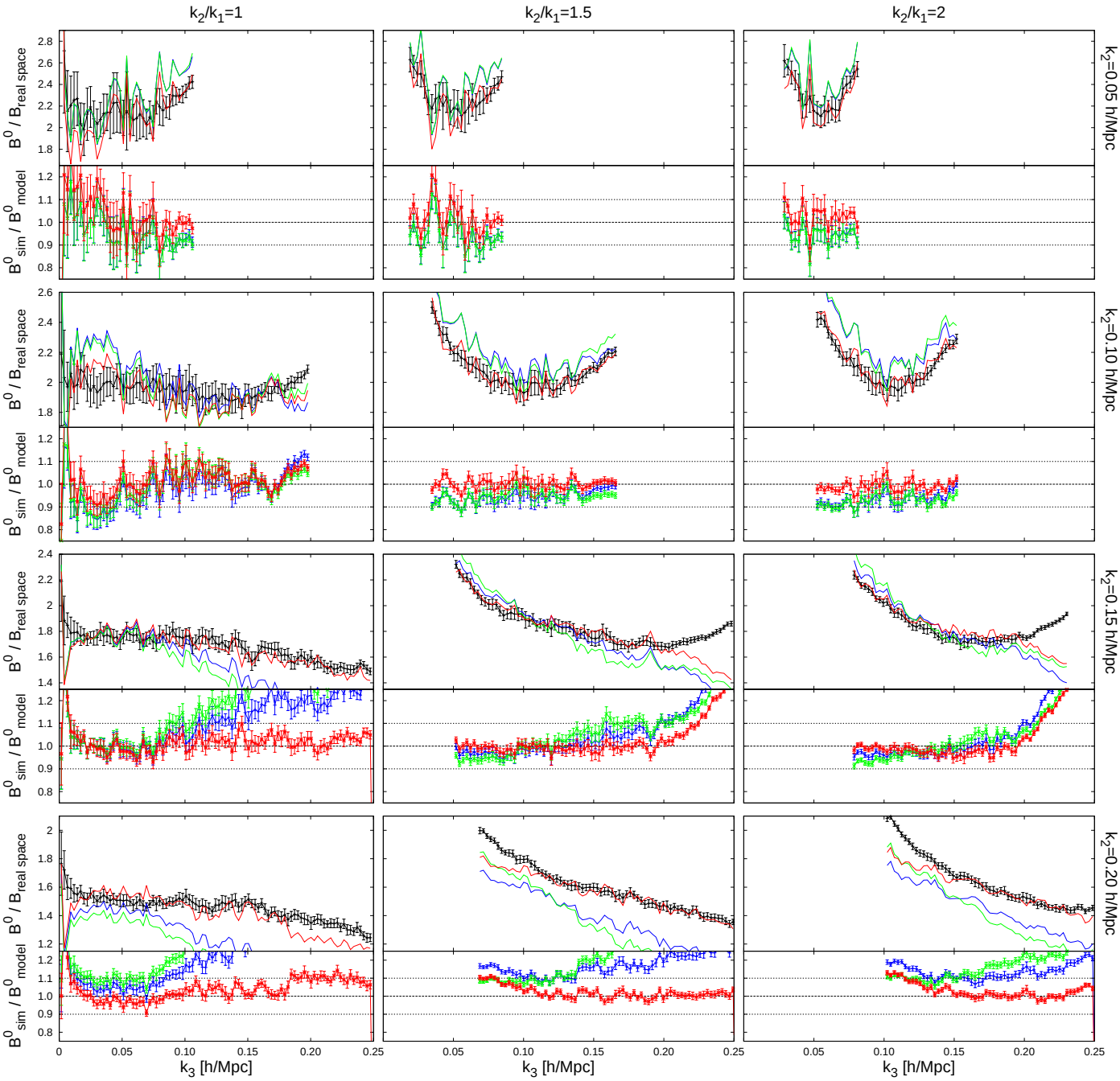


**Figure 4**. Same notation that in Fig. 3. All panels at $z = 0.5$.

to account for that, we use the prescription described in § 2.3.

We start by determining the bias parameters and $A_{\rm noise}$ from the real space power spectrum and bispectrum assuming fixed true values for $f$, $D(z)$, $\sigma_8$ and the shape of the linear power spectrum. In order to do so we apply the methodology described in § 2.4, using 20 realizations of N-body haloes. We use the model for real and redshift space power spectra described in § 2. We refer to these models as 2LRPT for real space and TNS-2LRPT for redshift space power spectrum.

For $k_{\rm max} = 0.15\,h/{\rm Mpc}$, when combining the power spectrum and bispectrum, we find that $b_1 = 2.05 \pm 0.014$, $b_2 = 0.31 \pm 0.05$, $A_{\rm noise} = 0.13 \pm 0.06$, where the error-bars correspond to the volume of one realization, $V_{\rm eff} = 3.375\,[{\rm Gpc}/h]^3$. We use these values as reference to test the accuracy

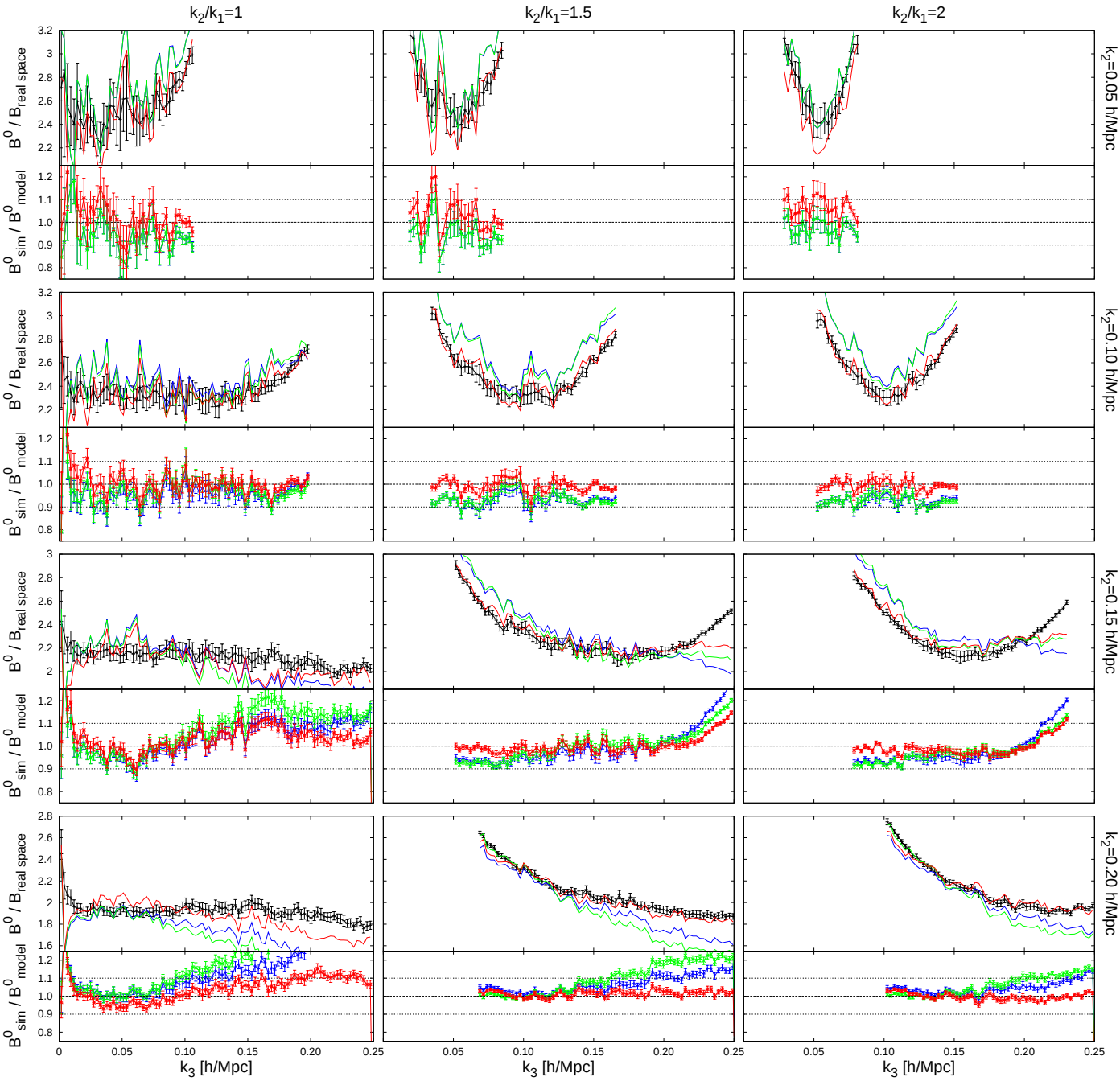


**Figure 5**. Same notation that in Fig. 3. All panels at $z = 1$.

of the description of the halo power spectrum and bispectrum in redshift space.

Fig. 7 presents a comparison between the measured power spectrum and the prediction of the model for $z = 0.55$. The real space power spectrum is displayed in the left panel (filled black circles). The redshift space power spectrum monopole and quadrupole are presented as empty black circles in the left and right panels respectively. These data are compared to the model for the real space power spectrum (blue line), monopole (red lines) and quadrupole (green lines). For the redshift space multipoles, the solid lines correspond to the assumption of $\sigma^P_{\rm fog} = 0$, whereas the dashed lines have $\sigma^P_{\rm fog}$ as free parameter. In this case, we find that $\sigma^P_{\rm fog} = 2.44\,{\rm Mpc}/h$ is the best-fitting value obtained from the monopole-to-quadrupole ratio. Therefore, we see the necessity of including a FoG-like damping

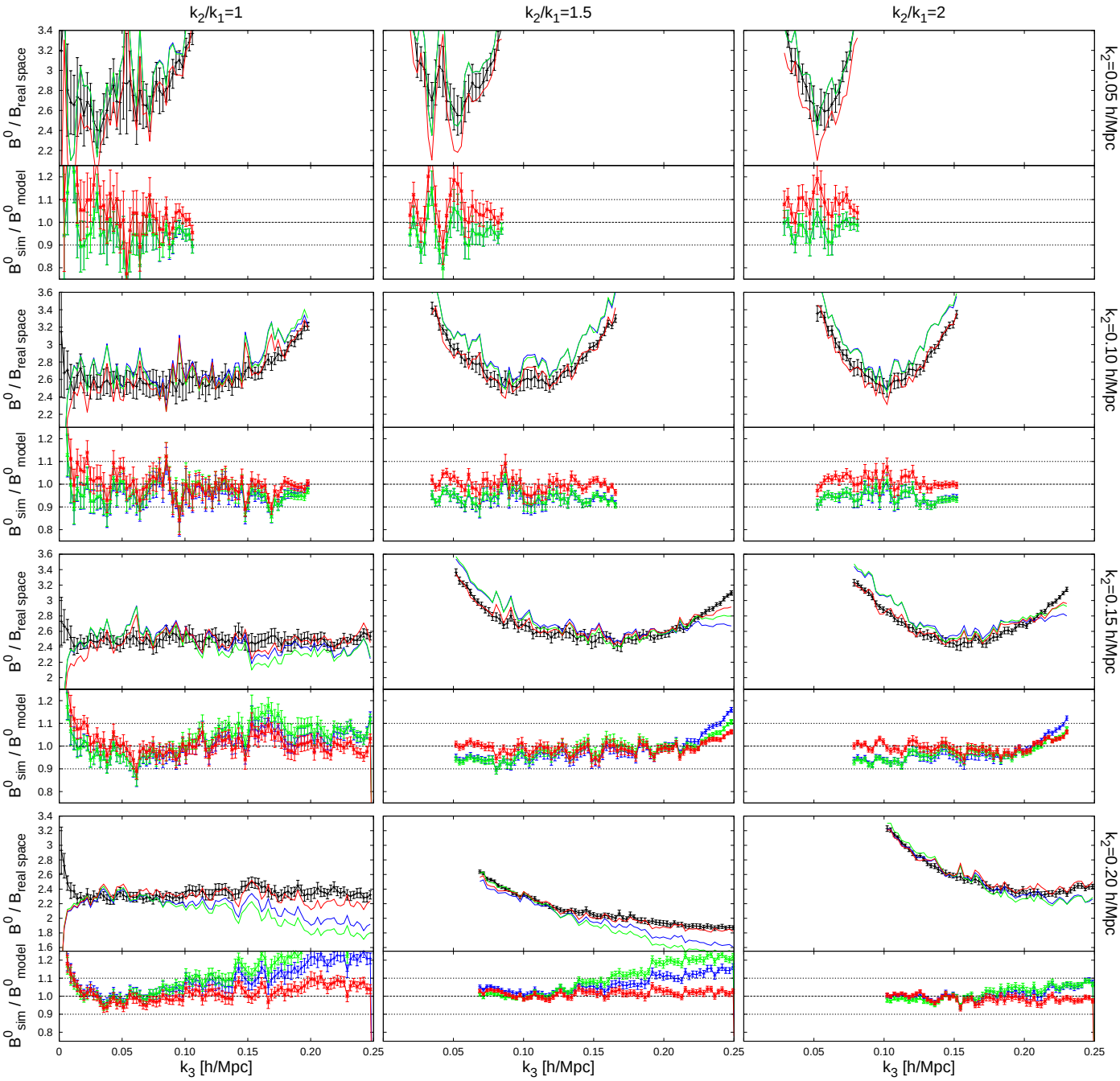


**Figure 6**. Same notation that in Fig. 3. All panels at $z = 1.5$.

term in the power spectrum even for describing the clustering of massive haloes. This feature was reported by the authors of the model [11]. When $\sigma^P_{\rm fog}$ is treated as a free parameter, the TNS-2LRPT model is able to reproduce the halo power spectrum monopole and quadrupole with a $\sim 4\%$ accuracy for $k \lesssim 0.22\,h/{\rm Mpc}$ at $z = 0.55$.

Fig. 8 presents the real-space halo bispectrum (black filled circles) and the redshift-space monopole halo bispectrum (black empty circles) for different scales and triangle shapes, as indicated in the different panels. We also show the prediction of the different models. The black solid line shows the real space prediction of Eq. 2.19 with the $F_2^{\rm eff}$ kernel of Eq. 2.21. The coloured lines show the bispectrum model predictions, $B^{\rm spt}$ (green lines) and $B^{\rm FG}$ (red lines), when $\sigma^B_{\rm fog} = 0$. Note that the bias param-

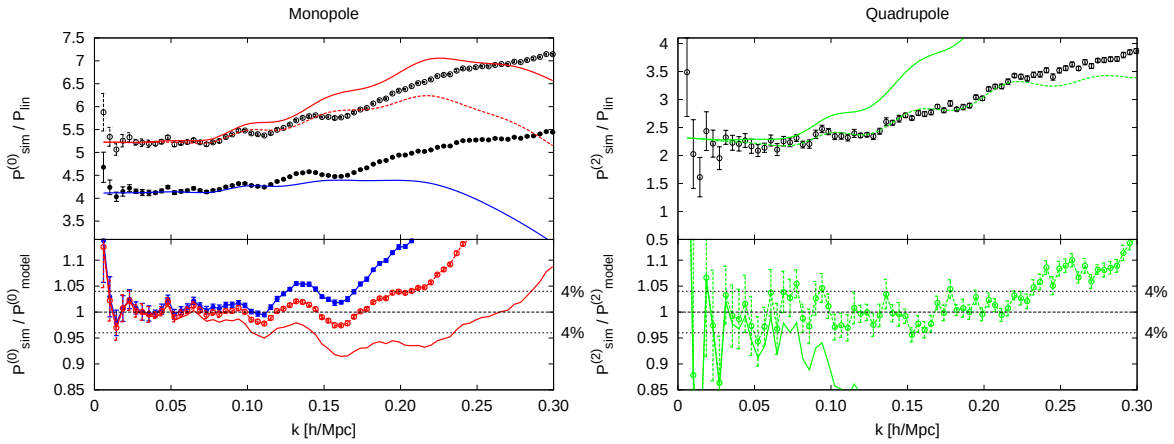


**Figure 7**. Top left: Halo power spectrum in real space (filled black circles) and power spectrum monopole (empty black circles) normalized to the linear model. In blue line the model for the real space power spectrum according to 2LRPT model (red lines). Top right: redshift space halo power spectrum quadrupole (open circles) and TNS-2LRPT (green lines). In both cases solid line corresponds to $\sigma^P_{\rm fog}$ is set to 0 and dashed line when $\sigma^P_{\rm fog}$ is set to 2.44 Mpc/$h$. In all the cases the bias parameters has been set to $b_1 = 2.05$, $b_2 = 0.31$ and the noise parameter $A_{\rm noise} = 0.13$. Bottom panels: Relative deviation between each model from top sub-panel and the measurement from N-body simulations.

eters and $A_{\rm noise}$ take the same value as for the power spectrum shown in Fig. 7. In general we see a moderate improvement for $B^{FG}$ over $B^{\rm spt}$ especially for folded triangles of the form $k_1 + k_2 \simeq k_3$ and $|k_1 - k_2| \simeq k_3$. Thus the set of $\mathbf{a}^G$ derived from dark matter is able to predict the halo bispectrum when $\sigma^P_{\rm fog}$ is set to 0. This suggests that, as the haloes do not have a FoG component, $\mathbf{a}^G$ does not contain any significant FoG feature.

We have seen that, for some configurations, $B^{FG}$ is able to describe with 5 to 10% percent error the halo bispectrum with the bias parameters derived from real spaces quantities. However, we are also interested into see whether the bias parameters estimated from redshift space statistics are similar to those obtained in real space.

In Fig 9 we apply the method from § 2.4 to estimate the best-fitting values of $b_1$, $b_2$ and $A_{\rm noise}$. Each dot corresponds to the set of parameters that minimize $\chi^2_{\rm diag.}$ for each of 20 realizations. The mean value and its dispersion corresponds to the estimator of the parameter set. These quantities are estimated from real space statistics (blue points) and redshift space statistics using $B^{\rm spt}$ (green points) and $B^{\rm FG}$ (red points). Left panels display the results using bispectrum information only, whereas the right panel combines power spectrum and bispectrum measurements. From the bispectrum only panels we see that the $B^{\rm FG}$ model (red points) agrees very well with the real space model (blue points) for the bias parameters $b_1$ and $b_2$, but $B^{\rm spt}$ (green points) tends to underestimate the value of $b_1$ and overestimate the value for $b_2$. Regarding the $A_{\rm noise}$ parameter, we see a small disagreement between the real and the redshift prediction even for the model $B^{\rm FG}$. This is not necessarily a problem since we expect an extra clustering in redshift space due to the redshift space distortions. This could mean that the noise is more super-Poisson than it is in real space, matching the trend observed. From the right panel of Fig. 9 we observe a similar behaviour between the two models: $B^{FG}$ is able to recover a $b_1$ consistent with the fit in real space. We see that there is a moderate discrepancy between the real and redshift-space predictions of $b_2$, where the prediction in redshift space tends to overestimate $b_2$ with respect to the real space prediction. Note that in this case, we allow $\sigma^P_{\rm fog}$ as a free parameter, although is not shown and $\sigma^B_{\rm fog}$ is always set to 0.

In Table 4, we provide the estimated values of the bias parameters, as well as $A_{\rm noise}$ and $\sigma^P_{\rm fog}$ corresponding to the right panel of Fig. 9. The left column corresponds to the (mean of the) blue distribution of points, the central column to the green, and the right column to the red in Fig. 9. The

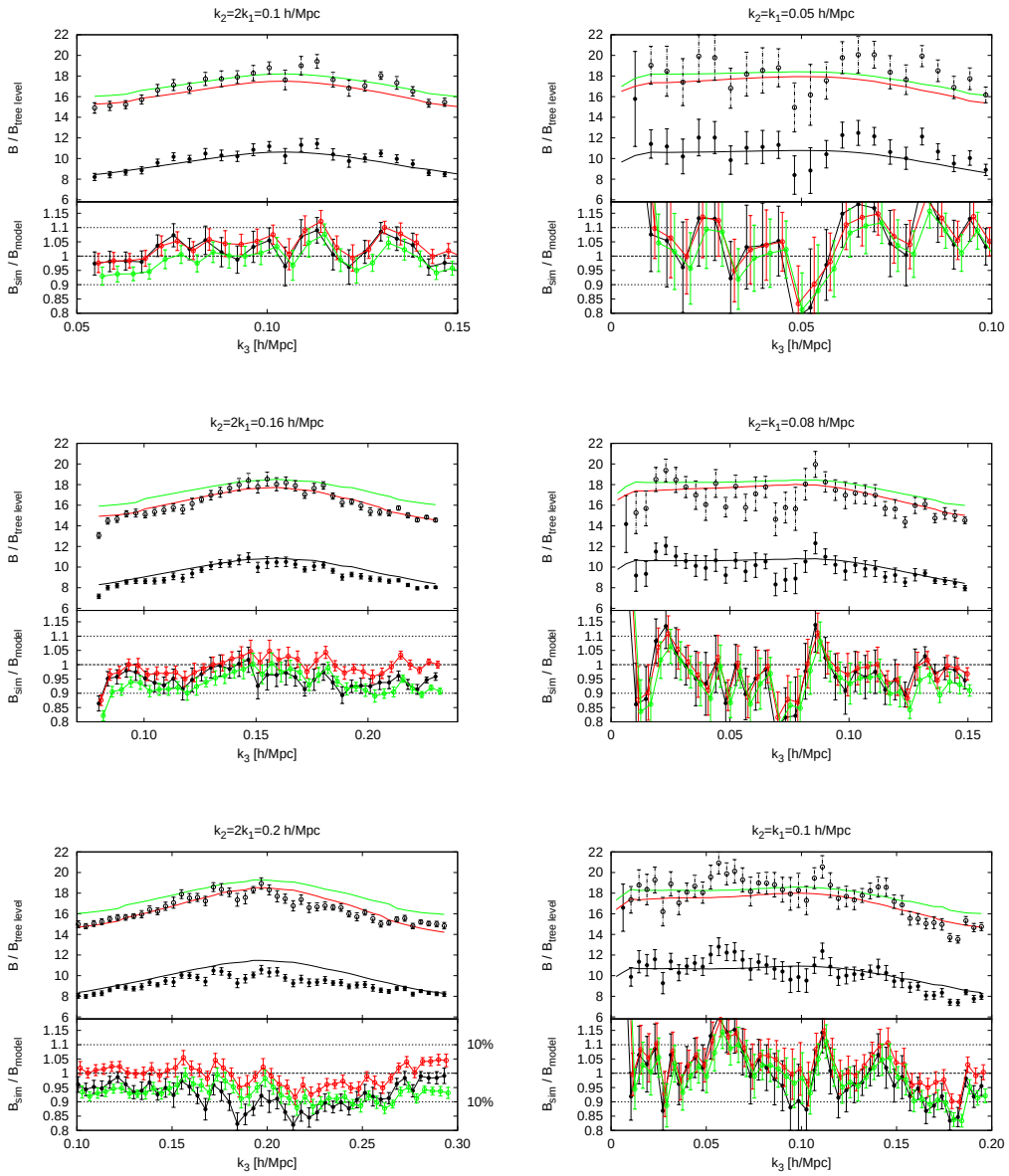


**Figure 8**. Top sub-panels: Halo bispectrum in real space (filled black circles) and bispectrum monopole (empty black circles) normalised to the tree-level prediction. Black solid line is the prediction for real space halo bispectrum according to the model of Eq. 2.19 with the $F_2^{\rm eff}$ kernel of Eq. 2.21. Green and red line are the predictions for the monopole halo bispectrum according to $B^{\rm spt}$ and $B^{FG}$ models respectively where the $\sigma^B_{\rm fog}$ parameter has been set to 0. Different panels show different triangular configuration as indicated at the top. Bottom sub-panels show the relative deviation of each model respect to the measurement from N-body haloes. The bias parameters and noise factor are the same that in Fig. 7. $z = 0.55$

error-bars correspond to $1\sigma$ of an effective volume of $V_{\rm eff} = 3.375\,h/{\rm Mpc}$. This enable us to quantify how the measurements of $b_1$ obtained with the $B^{\rm FG}$ model, compares with the real space predictions.

We conclude that the $B^{FG}$ model, with the set of $\mathbf{a}^G$ parameters presented in § 5, in combination with the TNS-2LRPT model for the redshift space power spectrum, is able to consistently recover the values of the bias parameters in real and redshift space when the power spectrum and bispectrum statistics are analysed. In particular, we find that if $B^{\rm spt}$ model is used instead, in redshift space $b_1$

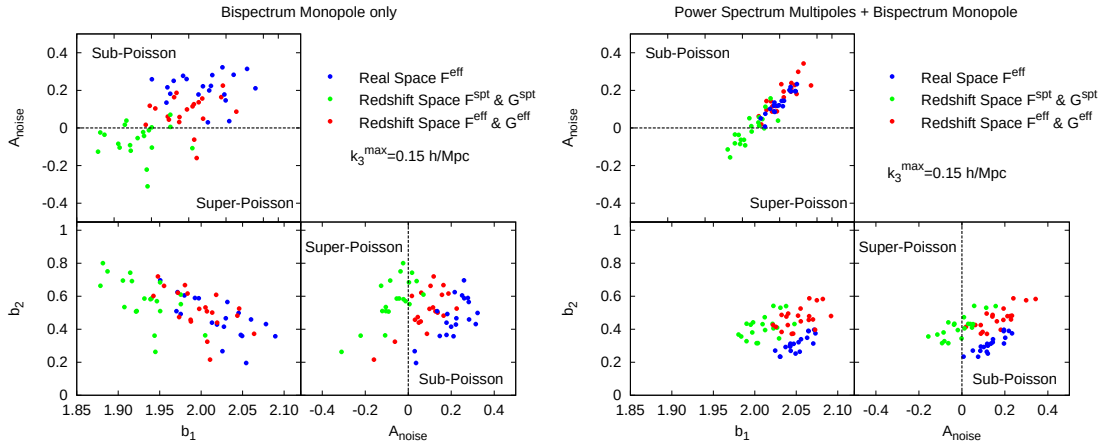


**Figure 9**. Best-fitting parameters from halo bispectrum only measurements (left panel) and from the combination of the power spectrum multipoles and bispectrum (right panel). Only $b_1$, $b_2$, $A_{\rm noise}$ and $\sigma^P_{\rm fog}$ are allowed to vary. Blue dots mark the best-fitting parameters from real space fits. Green and red points are the best-fitting parameters from redshift space using $B^{\rm spt}$ (green points) and $B^{\rm FG}$ (red points) for describing the bispectrum. Note that for the fits shown in the right panel, $\sigma^P_{\rm fog}$ was allowed to vary, although it is not shown for clarity. $f$ and $\sigma_8$ have been set to their true values.

| | Real Space | Redshift Space $B^{\rm spt}$ | Redshift Space $B^{\rm FG}$ |
|---|---|---|---|
| $b_1$ | $2.050 \pm 0.014$ | $2.011 \pm 0.018$ | $2.053 \pm 0.019$ |
| $b_2$ | $0.31 \pm 0.05$ | $0.41 \pm 0.07$ | $0.47 \pm 0.06$ |
| $A_{\rm noise}$ | $0.13 \pm 0.06$ | $-0.01 \pm 0.07$ | $0.17 \pm 0.08$ |
| $\sigma^P_{\rm fog}$ [Mpc/$h$] | 0 | $2.31 \pm 0.13$ | $2.44 \pm 0.12$ |

**Table 4**. Recovered parameters, $b_1$, $b_2$, $A_{\rm noise}$ and $\sigma^P_{\rm fog}$ for haloes, when the power spectrum and bispectrum are used. The different columns are measurements in real space (left column) and redshift space when $B^{\rm spt}$ and $B^{\rm FG}$ are used to describe the bispectrum (central and right column respectively). The maximum scale is set to $k_{\rm max} = 0.15\,h/{\rm Mpc}$. These values are in direct connection with the right panel of Fig. 9.

is underestimated.

## 7 Applications to cosmology

In this section we show how the $B^{\rm FG}$ model can be used to constrain $f$ and extract the bias parameters as well as $\sigma_8$ from power spectrum and bispectrum measurements. Combining the power spectrum multipoles and the bispectrum monopole allows us to disentangle the large scale degeneracy that typically ties $b_1$, $\sigma_8$ and $f$ together. In order to study these degeneracies, we start by recovering these parameters from dark matter fields. However, we are also interested in applying this technique to N-body haloes, which may suffer from different, and more realistic systematics errors.

### 7.1 Dark matter field

The different panels of Fig. 10 display the distributions of the best-fitting parameters values obtained from the dark matter N-body simulations for $z = 0.5$ and $k_{\rm max} = 0.15\,h/{\rm Mpc}$ when different statistics are used: power spectrum monopole and quadrupole (green symbols), power spectrum and bispectrum monopole (blue symbols) and power spectrum monopole, quadrupole and bispectrum monopole (red symbols). As in Fig. 9, we have applied the method of § 2.4, where each point corresponds to the set of parameters that minimizes $\chi^2_{\rm diag.}$ for a single realization. We consider as free parameters

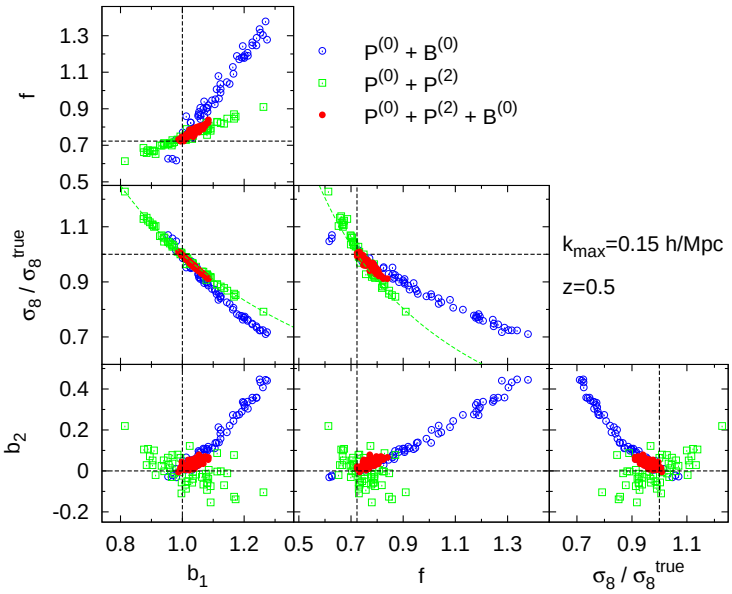


**Figure 10**. Best-fitting parameters for dark matter simulations in redshift space at $z = 0.5$ for $k_{\rm max} = 0.15$ when different statistics are used: blue points correspond to $P^{(0)} + B^{(0)}$, green points to $P^{(0)} + P^{(2)}$ and red points to $P^{(0)} + P^{(2)} + B^{(0)}$ as indicated. The dashed black lines mark the true values. The green dashed lines mark the $b_1 \propto \sigma_8^{-1}$ and the $f \propto \sigma_8^{-1}$ relations. Note that $b_1$, $b_2$, $f$, $\sigma_8$, $\sigma_0^P$, $\sigma_0^B$ are varied as free parameters, although only $b_1$, $b_2$, $f$ and $\sigma_8$ are shown for clarity.

$\{b_1, b_2, \sigma^P_{\rm fog}, \sigma^B_{\rm fog}, f, \sigma_8\}$. Note that we assume that the shot noise is given by Poisson statistics, hence $A_{\rm noise} = 0$. We have checked that for dark matter particles the role that $A_{\rm noise}$ plays is negligible, since the number density of particles is very high. For clarity, in Fig. 10 we only display the parameter-space projection for $\{b_1, b_2, \sigma_8, f\}$, which are the parameters we are interested in. The black dashed lines show the reference (true) values of the parameters. We see that when the power spectrum monopole and quadrupole are used, $f$, $\sigma_8$ and $b_1$ are only constrained in the following combinations: $f \sim \sigma_8^{-1}$ and $b_1 \sim \sigma_8^{-1}$. These relations can be analytically extracted by a simple inspection of the large scale limits of the model. We also notice that this is not the case for $b_2$, because it is a second-order parameter in the power spectrum. We also see that when the power spectrum and bispectrum monopole are used, the parameters are again constrained in combination, but the combination is different from the monopole-to-quadrupole case. Furthermore, we see that in this case, $b_2$ is also constrained only in combination with $\sigma_8$ and $b_1$. This is because in the bispectrum $b_2$ appears to leading order. Since these parameter combinations are different for $P^{(0)} + P^{(2)}$ (green symbols) and $P^{(0)} + B^{(0)}$ (blue symbols), we break the degeneracies between $b_1$, $b_2$, $\sigma_8$ and $f$ when we combine them all: $P^{(0)} + P^{(2)} + B^{(0)}$. In this case, we observe that the estimated parameters are close to their reference values (marked as black dashed lines), although there are small deviations. We are interested in quantifying these deviations for different redshifts, and also as a function of the maximum scale used for the analysis.

In Fig. 11 we present the estimates of $b_1$, $b_2$, $f$ and $\sigma_8$ as a function of $k_{\rm max}$ from 60 realizations of dark matter N-body simulations for $z = 0$ (red lines), $z = 0.5$ (blue lines), $z = 1$ (green lines) and $z = 1.5$ (orange lines), when the power spectrum monopole, quadrupole and bispectrum monopole are used. The error-bars correspond to $1\sigma$ dispersion of a realization of volume $V = 13.8\,[{\rm Gpc}/h]^3$. We only display error-bars for $z = 0.5$ for clarity, since the relative errors are similar for the other redshifts. The black dashed lines indicate the reference values of the parameters.

We observe that for the $z > 0$ redshift snapshots, the $b_1$ parameter is underestimated by $\sim 0.5\%$. For all redshifts , $b_2$ is overestimated by 0.05; $f$ is typically overestimated by $3 - 4\%$, whereas $\sigma_8$ is

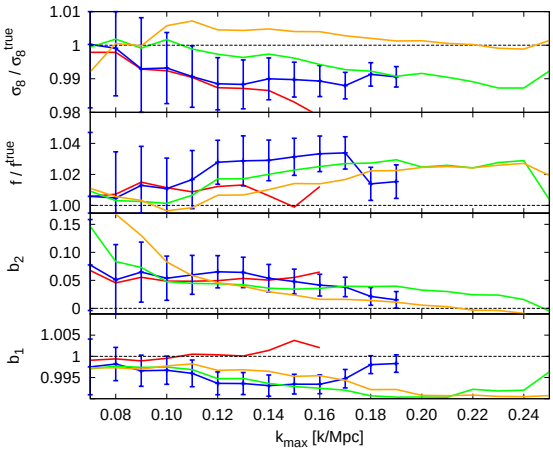


**Figure 11**. Parameters as a function of $k_{\rm max}$ obtained from combining the dark matter $P^{(0)}$, $P^{(2)}$ and $B^{(0)}$. Although only $b_1$, $b_2$, $\sigma_8$ and $f$ are shown, $\sigma_0^P$ and $\sigma_0^B$ are also varied in the fit. The colour indicate the redshift bin used: $z = 0$ (red), $z = 0.5$ (blue), $z = 1$ (green) and $z = 1.5$ (orange). Values are the mean of the best-fittings of the simulations and errors correspond to $1\sigma$ dispersion among simulations for an effective volume of $13.8\,[{\rm Gpc}/h]^3$. Error-bars are only shown for $z = 0.5$ for clarity; the relative errors are similar for the other redshifts. The black dashed lines are the reference values.

underestimated at some redshifts and overestimated at others, but typically by $\leq 1\%$.

To summarise, for dark matter particles, we are able to recover the correct bias parameters as well as $\sigma_8$ and the logarithmic growth factor with $\sim 1\%$ accuracy, when the power spectrum monopole and quadrupole are used in combination with the bispectrum monopole.

### 7.2 Dark matter haloes

In this section we aim to repeat the above analysis, but now for dark matter haloes. In this case we fix $\sigma^B_{\rm fog} = 0$, as we do not have FoG features for haloes, and we allow $A_{\rm noise}$ to be free. Therefore, the $\mathbf{\Psi}$ set of free parameters corresponds to $\{b_1, b_2, \sigma_0^P, A_{\rm noise}, f, \sigma_8\}$. Fig. 12 is similar to Fig. 10, but using the halo catalogue instead of dark matter particles. In this case, the redshift is $z = 0.55$ and, as before, the maximum scale used for the fit is $k_{\rm max} = 0.15\,h/{\rm Mpc}$.

From Fig. 12 we see that when the $P^{(0)} + P^{(2)}$ and $P^{(0)} + B^{(0)}$ statistics are used, degeneracies appear among the parameters $f$, $\sigma_8$ and $b_1$, in a similar way to the dark matter case. Adding a third statistic breaks the degeneracies. Fig. 12 shows that the best-fitting values for $f$ and $\sigma_8$ are slightly biased from the reference values, which are marked by black dashed lines.

In the left panel of Fig. 13 we show the mean values of $f$, $\sigma_8$, $b_1$ and $b_2$ as a function of $k_{\rm max}$ when all $P^{(0)}$, $P^{(2)}$ and $B^{(0)}$ are used. The black dashed lines, show the reference values: true values for $f$ and $\sigma_8$ and values of $b_1$ and $b_2$ estimated from the real space power spectrum and bispectrum when $f$ and $\sigma_8$ were fixed (which we refer to as reference values), as in § 6. In the right panel of Fig. 13, we have combined the variables into $f\sigma_8$, $b_1\sigma_8$ and $b_2\sigma_8$, using $P^{(0)} + P^{(2)} + B^{(0)}$ (red lines) as well as $P^{(0)} + P^{(2)}$ (green lines). In both panels, the error-bars correspond to $1\sigma$ with an effective volume of $3.375\,[{\rm Gpc}/h]^3$ and are estimated using the method described in § 2.4.

From the left panel of Fig. 13, we see that, for all $k_{\rm max}$ explored, $\sigma_8$ is under-estimated by $\sim 10\%$, whereas $f$ and $b_1$ are overestimated by $\sim 10\%$. Also $b_2$ is over estimated by about $\Delta b_2 \sim 0.4$ respect to the real space findings. We note a significant deviation of these parameters from their reference values compared to those obtained from dark matter particles in Figs. 10 - 11. The offsets may arise from the halo bias model that relates the dark matter field with the halo field, as well as the mapping between real and redshift space of biased tracers.

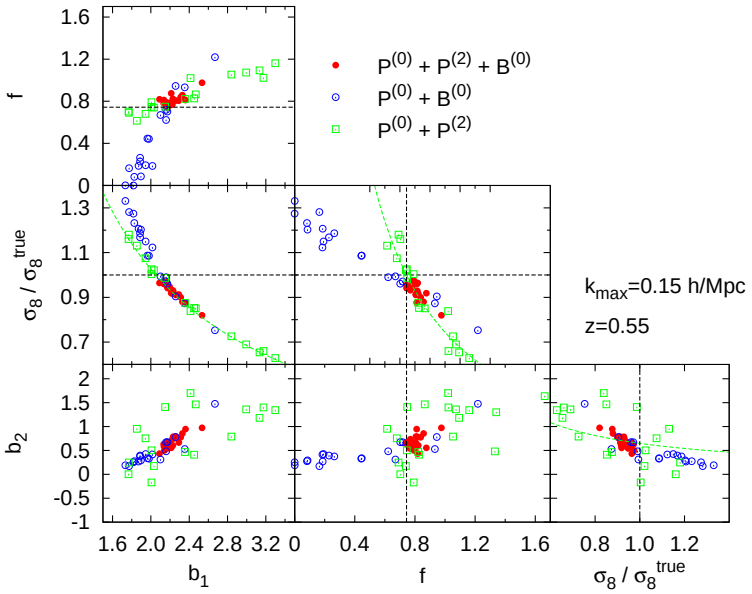


**Figure 12**. Same as Fig. 10 but for dark matter haloes at $z = 0.55$.

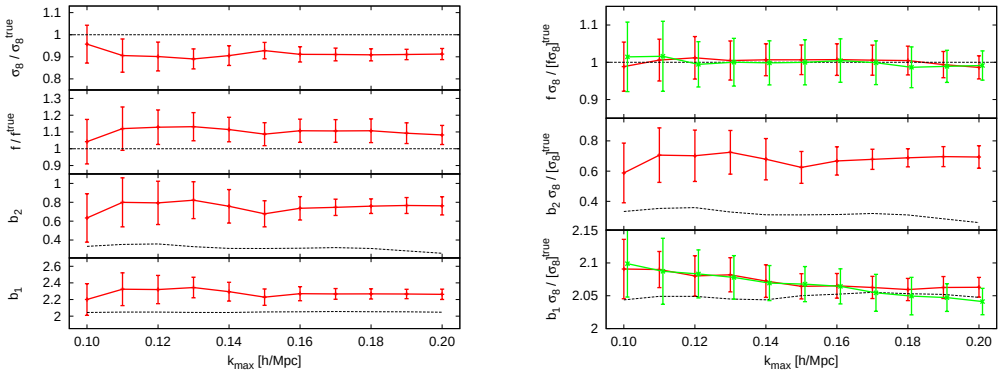


**Figure 13**. Left panel shows the best-fitting parameters for dark matter haloes as a function of $k_{\rm max}$ when $P^{(0)}$, $P^{(2)}$ and $B^{(0)}$ are jointly fitted. Although only $b_1$, $b_2$, $\sigma_8$ and $f$ are shown, $\sigma_0^P$ and $A_{\rm noise}$ are also varied in the fit. The right panel indicates the error of the combo variables $f\sigma_8$, $b_1\sigma_8$ and $b_2\sigma_8$ when $P^{(0)}$, $P^{(2)}$ and $B^{(0)}$ are used (red lines) and when $P^{(0)}$ and $P^{(2)}$ are used (green lines). Errors correspond to $1\sigma$ with an effective volume of $3.375\,[{\rm Gpc}/h]^3$. Black dotted lines show the true values for $\sigma_8$ and $f$, as well as the real-space values for $b_1$ and $b_2$ when $\sigma_8$ and $f$ are set to their true values.

Table 5 (second column) shows the results corresponding to the left panel of Fig. 13 for $k_{\rm max} = 0.15\,h/{\rm Mpc}$. Also shown (third column) are the results from real space (where $f$ and $\sigma_8$ have been fixed to their true values) for comparison, which are the dashed black lines in Fig. 13.

In the right panel of Fig. 13 we show the the predictions for the parameter combinations, $f\sigma_8$, $b_1\sigma_8$ and $b_2\sigma_8$ as a function of $k_{\rm max}$ estimated from $P^{(0)} + P^{(2)}$ (green lines) and $P^{(0)} + P^{(2)} + B^{(0)}$ (red lines). Since the combination $P^{(0)} + P^{(2)}$ is not able to estimate efficiently $b_2\sigma_8$, we do not show it in this case.

We note that neither $P^{(0)} + P^{(2)}$ nor $P^{(0)} + P^{(2)} + B^{(0)}$ present any significant offset on $f\sigma_8$ at any scale. On the other hand, a small systematic offset on $b_1\sigma_8$ is observed with respect to the

| $k_{\rm max} = 0.15\,h/{\rm Mpc}$ | $P^{(0)} + P^{(2)} + B^{(0)}$ | $P + B$ |
|---|---|---|
| $b_1$ | $2.23 \pm 0.10$ | $2.050 \pm 0.014$ |
| $b_2$ | $0.68 \pm 0.14$ | $0.31 \pm 0.05$ |
| $\sigma_8$ | $0.742 \pm 0.030$ | $0.80$ |
| $f$ | $0.809 \pm 0.051$ | $0.744$ |

**Table 5**. Recovered parameters, $b_1$, $b_2$, $f$ and $\sigma_8$ for haloes, when the power spectrum and bispectrum are used. The different columns are measurements in real space ("P+B" column) and redshift space when $P^{(0)}$, $P^{(2)}$ and $B^{(0)}$ are used. The maximum scale is set to $k_{\rm max} = 0.15\,h/{\rm Mpc}$. The measurements without error-bars are set to their true values.These values corresponds to the left panel of Fig. 13.

real space predictions, of order $1\sigma$ at small $k_{\rm max}$. Finally, $b_2\sigma_8$ presents a similar systematic to that observed for $b_2$ alone in the left panel. Therefore, we see that the systematic offsets reported for $b_1$, $\sigma_8$ and $f$ cancel almost perfectly when we work with $f\sigma_8$ and $b_1\sigma_8$. In this case, we see that the predictions from $P^{(0)} + P^{(2)}$ and $P^{(0)} + P^{(2)} + B^{(0)}$ are very similar and we quantify that, by adding the bispectrum monopole to the power spectrum monopole and quadrupole, the error on $f\sigma_8$ and $b_1\sigma_8$ reduces by $\sim 30 - 40\%$ at all scales.

Table 6 shows the results corresponding to the right panel of Fig. 13 when different parameters of interest, $b_1\sigma_8$, $b_2\sigma_8$ and $f\sigma_8$ are estimated from $P^{(0)} + P^{(2)}$ and $P^{(0)} + P^{(2)} + B^{(0)}$ for $k_{\rm max} = 0.15\,h/{\rm Mpc}$. We have normalised these quantities by the true values of $\sigma_8$ and $f$ for clarity.

| | $P^{(0)} + P^{(2)} + B^{(0)}$ | $P^{(0)} + P^{(2)}$ | $P + B$ |
|---|---|---|---|
| $b_1\sigma_8/[\sigma_8]^{\rm true}$ | $2.064 \pm 0.019$ | $2.068 \pm 0.027$ | $2.050 \pm 0.014$ |
| $b_2\sigma_8/[\sigma_8]^{\rm true}$ | $0.62 \pm 0.11$ | $0.66 \pm 0.43$ | $0.31 \pm 0.05$ |
| $f\sigma_8/[f\sigma_8]^{\rm true}$ | $1.007 \pm 0.040$ | $1.000 \pm 0.055$ | $1$ |

**Table 6**. Recovered parameters, $b_1\sigma_8$, $b_2\sigma$ and $f\sigma_8$ for haloes, when different statistics are used: first column $P^{(0)} + P^{(2)} + B^{(0)}$, second column $P^{(0)} + P^{(2)}$ and third column $P + B$ (real space quantities with $f$ and $\sigma_8$ set to true values). The maximum scale is set to $k_{\rm max} = 0.15\,h/{\rm Mpc}$. The numbers without error-bars are set to their true values. Numbers in this table correspond to the right panel of Fig. 13.

## 8 Conclusions

The main goal of this paper is to provide an empirical formula for the redshift space bispectrum monopole for the dark matter field and for biased tracers such as galaxies or haloes. The statistical power of present and forthcoming surveys imply that the accuracy of existing analytic descriptions is not sufficient considering the statistical power of current surveys. The bispectrum statistic offers additional complementary information to that contained in the power spectrum multipoles, which, in principle, helps reduce error-bars and break degeneracies among cosmological parameters.

Here (§ 5) we have extended the real space dark matter bispectrum formula presented in [1] to account for the redshift-space distortions at the level of the bispectrum monopole. We refer to this new formula as $B^{FG}$. We have proceeded by modifying the standard perturbation theory velocity kernel $G_2$ to an effective kernel $G_2^{\rm eff}$ with nine free parameters, $\mathbf{a}^G$. We have constrained the values of these parameters using measurements of the redshift space bispectrum monopole from dark matter N-body simulations (for a total effective volume of $\sim 829[{\rm Gpc}/h]^3$) at four different redshift, $z = 0\,, 0.5\,, 1.0\,, 1.5$. With this, $B^{FG}$ is able to describe the dark matter bispectrum monopole in redshift space with a precision of $\lesssim 5\%$ for $k \leq 0.10\,h/{\rm Mpc}$ at $z = 0$; for $k \leq 0.15\,h/{\rm Mpc}$ at $z = 0.5$; for $k \leq 0.17\,h/{\rm Mpc}$ at $z = 1.0$ and for $k \leq 0.20\,h/{\rm Mpc}$ at $z = 1.5$.

We have proceeded to combine the predictions of $B^{FG}$, with the non-local and non-linear bias model [12], in order to provide a theoretical description of the bispectrum in redshift space for dark matter haloes (§ 6). We find that $B^{FG}$ provides a better description of the halo bispectrum in redshift

space than the standard perturbation theory leading order prediction. In this case $B^{FG}$ predicts with a $\lesssim 5\%$ accuracy the halo bispectrum in redshift space for $k \lesssim 0.15\,h/\mathrm{Mpc}$ at $z = 0.55$. For comparison, the SPT approach would perform similarly only up to $k \lesssim 0.06$: in other words, the extension reduces the statistical error-bars as much as it would increasing the survey volume by a factor of four.

To demonstrate the power of adding the bispectrum information to the power spectrum, we have combined the bispectrum model $B^{FG}$ with the power spectrum monopole and quadrupole model of [11] and [36]. First we have extracted the bias parameters $b_1$ and $b_2$ from simulations when other cosmological parameters such as $f$ and $\sigma_8$ were fixed to their true values. We have found that $B^{FG}$ is able to predict the same large scale bias parameter, $b_1$ in real and redshift space, whereas standard perturbation theory approach for the redshift space kernel underestimates $b_1$ in redshift space with respect to real space by 2% (this is large enough to be statistically significant given the size of the simulations). We have further explored the performance of the modelling proposed here in extracting $f$, $\sigma_8$ as well as the bias parameters $b_1$ and $b_2$ from the power spectrum monopole, $P^{(0)}$, quadrupole, $P^{(2)}$ and the bispectrum monopole, $B^{(0)}$ (§ 7). Our main findings are as follows:

1. For the dark matter field no systematics offsets larger than 1% are found for $b_1$, $b_2$ and $f$ when $P^{(0)}$, $P^{(2)}$ and $B^{(0)}$ are used.

2. For the dark matter halo catalogue, when the parameters $\{b_1, b_2, f, \sigma_8\}$ are estimated from $P^{(0)} + P^{(2)}$, no systematic offsets appear for $f\sigma_8$ and a $\sim 1\%$ systematic error is found for $b_1\sigma_8$ with respect to the real space prediction. If we add $B^{(0)}$ to these two statistics, the errors on $f\sigma_8$ and $b_1\sigma_8$ combinations are reduced by about $\sim 30 - 40\%$, regardless of the value of $k_{\mathrm{max}}$ and no additional systematic errors are evident. Adding $B^{(0)}$ allow us to measure also $b_2\sigma_8$. In this case we do find a systematic error of $\sim 50\%$ compared to the real space prediction.

3. Combining $P^{(0)}$, $P^{(2)}$ and $B^{(0)}$ allows us also to estimate the variables $b_1$, $f$ and $\sigma_8$ separately. In this case we find that $b_1$ and $f$ are underestimated by $\sim 10\%$ and $\sigma_8$ is overestimated by a similar amount for $0.10 \leq k_{\mathrm{max}}\,[h/\mathrm{Mpc}] \leq 0.20$. Note that for the dark matter case these systematics were smaller than 1%.

4. It is likely that the systematics found for $f$, $b_1$ and $\sigma_8$ are due to a limitation of the halo bias modelling when describing the power spectrum and bispectrum in redshift space. These systematics can be tamed if we work with the combinations $f\sigma_8$ and $b_1\sigma_8$.

The bispectrum fitting formula presented in this paper may be useful for and directly applicable to any galaxy survey when redshift space distortions in the bispectrum must be accounted for.

While there is no evidence for important systematic effects in the combination $f\sigma_8$, the combination of power spectrum monopole and quadrupole and the bispectrum monopole allow us to break the degeneracy between $f$ and $\sigma_8$ but systematic shifts of $\sim 10\%$ appear, which are of the order of the statistical errors for current state-of-the-art surveys. Using instead the power spectrum and bispectrum monopoles, a *different* combination of $f$-$\sigma_8$ is measured. This new combination also presents systematic shifts, but smaller, less than 10%.

Clearly more work, especially in understanding the interplay between biasing and redshift-space distortions and their combined effects on clustering, is needed in order to reduce these systematic shifts and bring them below the statistical errors.

## Acknowledgments

We thank Beth Reid for providing the N-body halo catalogues used in this paper.

HGM is grateful for support from the UK Science and Technology Facilities Council through the grant ST/I001204/1. LV is supported by European Research Council under the European Communities Seventh Framework Programme grant FP7-IDEAS-Phys.LSS and acknowledges Mineco grant FPA2011-29678- C02-02. WJP is grateful for support from the UK Science and Technology Facilities Research Council through the grant ST/I001204/1, and the European Research Council through the grant Darksurvey.

Numerical computations were done on Hipatia ICC-UB BULLx High Performance Computing Cluster at the University of Barcelona. The simulations for N-body haloes used in this § 6 of this paper were analysed at the National Energy Research Scientific Computing Center, the Shared Research Computing Services Pilot of the University of California and the Laboratory Research Computing project at Lawrence Berkeley National Laboratory.

## References

[1] Gil-Marín, H., Wagner, C., Fragkoudi, F., Jimenez, R., & Verde, L. 2012, *J. Cosmology Astropart. Phys.*, 2, 47

[2] Eisenstein, D. J., Weinberg, D. H., Agol, E., et al. 2011, *AJ*, 142, 72

[3] Drinkwater, M. J., Jurek, R. J., Blake, C., et al. 2010, *MNRAS*, 401, 14

[4] The Dark Energy Survey Collaboration 2005, arXiv:astro-ph/0510346

[5] Laureijs, R., Amiaux, J., Arduini, S., et al. 2011, arXiv:1110.3193

[6] Crocce, M., & Scoccimarro, R. 2006, *Phys. Rev. D*, 73, 063519

[7] Okamura, T., Taruya, A., & Matsubara, T. 2011, *J. Cosmology Astropart. Phys.*, 8, 12

[8] Carlson, J., Reid, B., & White, M. 2013, *MNRAS*, 429, 1674

[9] Pietroni, M. 2008, *J. Cosmology Astropart. Phys.*, 10, 36

[10] Valageas, P., & Nishimichi, T. 2011, *A&A*, 532, A4

[11] Nishimichi, T., & Taruya, A. 2011, *Phys. Rev. D*, 84, 043526

[12] McDonald, P., & Roy, A. 2009, *J. Cosmology Astropart. Phys.*, 8, 20

[13] Saito, S., Baldauf, T., Vlah, Z., et al. 2014, arXiv:1405.1447

[14] Vlah, Z., Seljak, U., McDonald, P., Okumura, T., & Baldauf, T. 2012, *J. Cosmology Astropart. Phys.*, 11, 9

[15] Okumura, T., Seljak, U., & Desjacques, V. 2012, *J. Cosmology Astropart. Phys.*, 11, 14

[16] Taruya, A., Nishimichi, T., & Saito, S. 2010, *Phys. Rev. D*, 82, 063522

[17] Reid, B. A., & White, M. 2011, *MNRAS*, 417, 1913

[18] Scoccimarro, R., Colombi, S., Fry, J. N., et al. 1998, *ApJ*, 496, 586

[19] Pan, J., Coles, P., & Szapudi, I. 2007, *MNRAS*, 382, 1460

[20] Sefusatti, E. 2009, *Phys. Rev. D*, 80, 123002

[21] Yokoyama, S., Matsubara, T., & Taruya, A. 2014, *Phys. Rev. D*, 89, 043524

[22] Takushima, Y., Terukina, A., & Yamamoto, K. 2014, *Phys. Rev. D*, 89, 104007

[23] Verde, L., & Heavens, A. F. 2001, *ApJ*, 553, 14

[24] Jürgens, G., & Bartelmann, M. 2012, arXiv:1204.6524

[25] Rampf, C., & Buchert, T. 2012, *J. Cosmology Astropart. Phys.*, 6, 21

[26] Angulo, R. E., Foreman, S., Schmittfull, M., & Senatore, L. 2014, arXiv:1406.4143

[27] Baldauf, T., Mercolli, L., Mirbabayi, M., & Pajer, E. 2014, arXiv:1406.4135

[28] Albrecht, A., Bernstein, G., Cahn, R., et al. 2006, arXiv:astro-ph/0609591

[29] Amendola, L., Appleby, S., Bacon, D., et al. 2013, Living Reviews in Relativity, 16, 6

[30] Jennings, E., Baugh, C. M., Li, B., Zhao, G.-B., & Koyama, K. 2012, *MNRAS*, 425, 2128

[31] Beutler, F., Saito, S., Seo, H.-J., et al. 2013, arXiv:1312.4611

[32] Baldauf, T., Seljak, U., Desjacques, V., & McDonald, P. 2012, *Phys. Rev. D*, 86, 083540

[33] Chan, K. C., Scoccimarro, R., & Sheth, R. K. 2012, *Phys. Rev. D*, 85, 083509

[34] Davis, M., & Peebles, P. J. E. 1983, *ApJ*, 267, 465

[35] Jackson, J. C. 1972, *MNRAS*, 156, 1P

[36] Gil-Marín, H., Wagner, C., Verde, L., Porciani, C., & Jimenez, R. 2012, *J. Cosmology Astropart. Phys.*, 11, 29

[37] Jain, B., & Bertschinger, E. 1994, *ApJ*, 431, 495

[38] Scoccimarro, R., & Couchman, H. M. P. 2001, *MNRAS*, 325, 1312

[39] Catelan, P., Lucchin, F., Matarrese, S., & Moscardini, L. 1995, *MNRAS*, 276, 39

[40] Scoccimarro, R., Couchman, H. M. P., & Frieman, J. A. 1999, *ApJ*, 517, 531

[41] Verde, L., Heavens, A. F., Matarrese, S., & Moscardini, L. 1998, *MNRAS*, 300, 747

[42] Bernardeau, F., Colombi, S., Gaztañaga, E., & Scoccimarro, R. 2002, *Phys. Rep.*, 367, 1

[43] Hivon, E., Bouchet, F. R., Colombi, S., & Juszkiewicz, R. 1995, *A&A*, 298, 643

[44] Matsubara, T. 2007, *ApJS*, 170, 1

[45] Matarrese, S., Verde, L., & Heavens, A. F. 1997, *MNRAS*, 290, 651

[46] Verde, L., Heavens, A. F., Percival, W. J., et al. 2002, *MNRAS*, 335, 432

[47] Press, W. H., Teukolsky, S. A., Vetterling, W. T., & Flannery, B. P. 1992, Cambridge: University Press, —c1992, 2nd ed.,

[48] White, M., Blanton, M., Bolton, A., et al. 2011, *ApJ*, 728, 126

[49] Lewis, A., Challinor, A., & Lasenby, A. 2000, *ApJ*, 538, 473

[50] Springel, V. 2005, *MNRAS*, 364, 1105

[51] Davis, M., Efstathiou, G., Frenk, C. S., & White, S. D. M. 1985, *ApJ*, 292, 371